Monthly Notices
of the
ROYAL ASTRONOMICAL SOCIETY

MNRAS **478,** 4101–4127 (2018)
Advance Access publication 2018 May 5

doi:10.1093/mnras/sty1185

Uncertainties in s-process nucleosynthesis in low-mass stars determined from Monte Carlo variations

G. Cescutti,[1★†] R. Hirschi,[2,3†] N. Nishimura,[4†] J. W. den Hartogh,[2,5†] T. Rauscher,[6,7†] A. St. J. Murphy[8†] and S. Cristallo[9,10]

[1]*INAF, Osservatorio Astronomico di Trieste, I-34131 Trieste, Italy*
[2]*Astrophysics group, Lennard-Jones Laboratories, Keele University, ST5 5BG Staffordshire, UK*
[3]*Kavli Institute for the Physics and Mathematics of the Universe (WPI), University of Tokyo, 5-1-5 Kashiwanoha, Kashiwa 277-8583, Japan*
[4]*Yukawa Institute for Theoretical Physics, Kyoto University, Kyoto 606-8502, Japan*
[5]*Konkoly Observatory, Konkoly Thege Miklós út 15-17, H-1121 Budapest, Hungary*
[6]*Department of Physics, University of Basel, Klingelbergstr. 82, CH-4056 Basel, Switzerland*
[7]*Centre for Astrophysics Research, University of Hertfordshire, College Lane, Hatfield AL10 9AB, UK*
[8]*SUPA, School of Physics and Astronomy, University of Edinburgh, Edinburgh EH9 3FD, UK*
[9]*INAF, Osservatorio Astronomico d'Abruzzo, I-64100 Teramo, Italy*
[10]*INFN-Sezione di Perugia, I-06123 Perugia, Italy*

Accepted 2018 May 3. Received 2018 May 3; in original form 2017 November 8

ABSTRACT

The main s-process taking place in low-mass stars produces about half of the elements heavier than iron. It is therefore very important to determine the importance and impact of nuclear physics uncertainties on this process. We have performed extensive nuclear reaction network calculations using individual and temperature-dependent uncertainties for reactions involving elements heavier than iron, within a Monte Carlo framework. Using this technique, we determined the uncertainty in the main s-process abundance predictions due to nuclear uncertainties linked to weak interactions and neutron captures on elements heavier than iron. We also identified the key nuclear reactions dominating these uncertainties. We found that β-decay rate uncertainties affect only a few nuclides near s-process branchings, whereas most of the uncertainty in the final abundances is caused by uncertainties in neutron-capture rates, either directly producing or destroying the nuclide of interest. Combined total nuclear uncertainties due to reactions on heavy elements are in general small (less than 50 per cent). Three key reactions, nevertheless, stand out because they significantly affect the uncertainties of a large number of nuclides. These are ^{56}Fe(n,γ), ^{64}Ni(n,γ), and ^{138}Ba(n,γ). We discuss the prospect of reducing uncertainties in the key reactions identified in this study with future experiments.

Key words: nuclear reactions, nucleosynthesis, abundances – stars: abundances – stars: AGB and post-AGB – stars: evolution – stars: low-mass.

1 INTRODUCTION

Elements heavier than iron are mainly produced via neutron captures because the significant Coulomb barrier of these elements inhibits charged-particle captures. It is well established that the astrophysical origin of the majority of nuclides beyond Fe requires at least two neutron-capture processes (Burbidge et al. 1957; Cameron 1957), the so-called slow process (s-process) and rapid process (r-process): for the s-process the neutron-capture time-scale is generally longer than the β-decay time, whereas the opposite is true for the r-process.

In this work, we focus on the main component of the s-process, which takes place during the asymptotic giant branch (AGB) phase in low-mass stars, see e.g. Busso et al. (2001), Abia et al. (2002), Sneden, Cowan & Gallino (2008), and Zamora et al. (2009). The main neutron source for the s-process is the reaction ^{13}C(α,n)^{16}O (for a review of the main s-process, see Käppeler et al. 2011). This reaction is activated during the thermally pulsing AGB phase, taking place after central helium burning in low-mass stars. During this phase, energy production is dominated by the burning hydrogen shell and the helium shell flash events (thermal pulses, TPs), first described by Schwarzschild & Härm (1965). The TP starts when enough helium has been deposited by the hydrogen burning shell on top of the degenerate CO core and the helium shell becomes

★ E-mail: gabriele.cescutti@inaf.it
† BRIDGCE UK Network; www.bridgce.ac.uk

compressed and heated, see Herwig (2005). The helium shell ignites in an explosive way as the layers are degenerate, leading to a large energy flux and the extinction of the hydrogen burning shell. This large energy flux creates the pulse-driven convective zone (PDCZ) in the intershell, the area in between the core and the helium shell, which is expanding as a result of this energy flux. The expansion cools the region, allowing the helium shell to cool. The helium shell is now burning helium in a stable radiative manner until it runs out of fuel again. While the intershell region expands and cools, the convective envelope deepens. If the convective zone reaches sufficiently deep layers, it dredges up material enriched by the last PDCZ, a process called third dredge-up (TDU). Afterwards, the hydrogen shell re-ignites and the whole cycle repeats itself until the entire hydrogen-rich envelope has been lost by stellar winds. At the deepest point of penetration of the convective envelope, fresh protons are injected in the intershell, which is rich in ^{12}C. Incomplete CNO cycling leads to a significant production of ^{13}C in a narrow region below the convective envelope, which is often referred to as the ^{13}C-pocket, see Gallino et al. (1998), Herwig (2005), Straniero, Gallino & Cristallo (2006), and the first description by Iben (1976) for more details. As this region later contracts as the TP cycle proceeds, it heats up and a large number of neutrons are released by the neutron source reaction ^{13}C(α,n)^{16}O in a radiative (non-convective) layer (Straniero et al. 1995). A smaller contribution to the neutron flux comes from the ^{22}Ne(α,n)^{25}Mg neutron source, which is activated in intermediate-mass stars at the bottom of the PDCZ (Abia et al. 2001) and, thus, releases neutrons in a convective environment. We will refer to the PDCZ phase as 'TP' phase in the rest of the paper.

Low-mass AGB stars are the sites for the main component of the s-process, i.e. elements between strontium and lead. The second component of the s-process (called weak component) takes place at the end of core helium burning and at the start of carbon (shell) burning in massive stars. Typically, it produces elements up to the Sr peak but depending on the metallicity and the mixing induced by rotation can also produce heavier nuclides (see Cescutti et al. 2016; Frischknecht et al. 2016; Prantzos et al. 2018). The neutron source for the weak s-process is ^{22}Ne(α,n)^{25}Mg.

There are several well-known uncertainties concerning the s-process production in low-mass stars. On the astrophysical side, the most important one is the general properties of the ^{13}C-pocket and in particular its formation, see Cristallo et al. (2015), Battino et al. (2016), and Trippella et al. (2016) for a discussion and references. On the nuclear reaction side, Koloczek et al. (2016) (Ko16 hereinafter), recently reviewed the impact of current nuclear uncertainties considering both the ^{13}C-pocket and TP conditions. As expected, they identify the neutron source reactions mentioned above as key reactions. They find that their uncertainties strongly affect the s-process production as do the competing reactions [see e.g. the discussion in Nishimura et al. 2014, for ^{22}Ne(α, γ)^{26}Mg]. Neutron poison reactions, such as ^{14}N(n,p), ^{13}C(n,γ), ^{16}O(n,γ), and ^{22}Ne(n,γ) for the ^{13}C-pocket conditions, and ^{22}Ne(n,γ) and ^{25}Mg(n,γ) for the TP conditions, were also found to have a strong effect. The Ko16 study also identified a wide range of neutron captures as well as a few weak reactions on elements heavier than and including iron. When varying charged-particle reactions on light nuclides (as done in the Ko16 study), it may be necessary to conduct these sensitivity studies using full stellar evolution models. For instance, the adoption of a lower rate for the ^{13}C(α,n) ^{16}O reaction could lead to the ingestion of some unburnt ^{13}C in the PDCZ, with important consequences on the ongoing s-process nucleosynthesis (Cristallo et al. 2018). In this study, we only explore uncertainties in neutron captures and beta-decays on intermediate and heavy isotopes. We thus do not expect feedback effects from rate variations on the structure and the adopted post-processing approach is appropriate. Our approach to vary reaction rates is different from that of Ko16. We vary simultaneously all reaction rates in a Monte Carlo (MC) framework rather than one reaction at a time. Furthermore, we use temperature-dependent uncertainties based both on experimental and theoretical studies as we have already done for several other processes: the s-process in massive stars, γ-process in core collapse SNe, and γ-process in supernovae type Ia (Rauscher et al. 2016; Nishimura et al. 2017; Nishimura et al. 2018). We will compare our findings to those of Ko16 and comment further on similarities and differences of methods and results in the discussion section.

The paper is organized in the following way. In Section 2, we describe the astrophysical model used in this study as well as the MC framework PizBuin. In Section 3, we present the results of our sensitivity study and the list of key rates identified. We also discuss these key rates and the prospects to reduce their uncertainties with future experiments. In Section 4, we give our conclusions.

2 METHODS

In this section, we describe the main ingredients of our calculations: the thermodynamic trajectories used for the ^{13}C-pocket, the TP phase, and the MC PizBuin framework. The basic features of s-process nucleosynthesis and the uncertainties of (n,γ) and weak rates determination are also summarized.

2.1 Astrophysical model

The complete evolution of low-mass stars is complex, especially during the TP-AGB phase. A full one-dimensional (1D) stellar model can require more than 100 000 time-steps and over one thousand spatial zones to be simulated completely from start to finish. It is thus not feasible to repeat such simulations 10 000 times as required by the MC procedure to complete a sensitivity study. We thus have to approximate the thermodynamic conditions inside the star with a trajectory following the key phase that we are studying. We start with the ^{13}C-pocket case. The fact that this phase occurs under radiative conditions (rather than convective) makes it feasible to approximate it with a carefully selected single trajectory. This trajectory does not follow exactly what happens in real stars but, as shown below, provides the conditions that lead to an s-process production similar to that predicted using full stellar models.

The trajectory used in this work was extracted from a 3 $M_{\odot}$, $Z = 0.014$ (solar metallicity) stellar evolution model, calculated with MESA, revision number 6208 (Paxton et al. 2011). The trajectory was taken from the ^{13}C-pocket following the 6th TP. The temperature and density profiles of the trajectory are shown in Fig. 1.

The trajectory starts after the ^{13}C-pocket has formed. The formation of the ^{13}C-pocket is the main uncertainty on the astrophysical side as mentioned above. The most advanced 3D models of stellar evolution are starting to resolve this phase in detail and Battino et al. (2016) have shown that using prescriptions in 1D stellar models guided by these 3D hydro simulations gives promising results. Most nucleosynthesis computations to date, however, typically take into account the ^{13}C-pocket either by directly inserting a specific proton abundance profile below the convective envelope (e.g. Karakas & Lugaro 2016) or by assuming the mixing process that leads to it (Cristallo et al. 2011; Trippella et al. 2016). In this study, we artificially increase the ^{13}C abundance, mimicking in this way the enhancement of ^{13}C due to the injection of protons. We explored

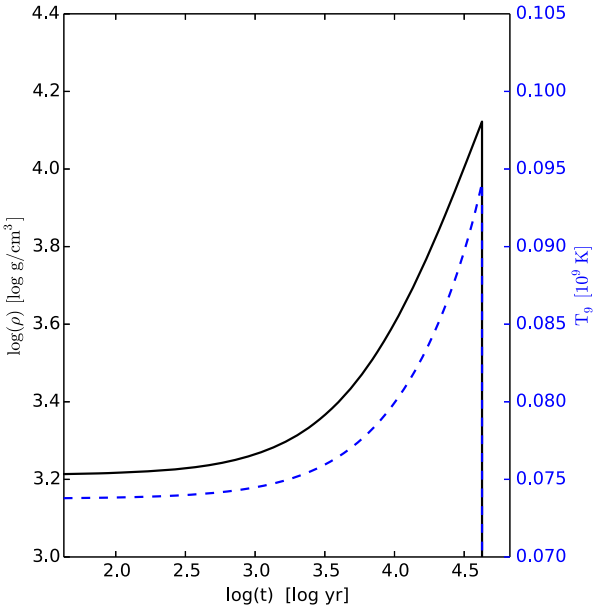

Figure 1. Time evolution of the temperature (GK) (blue dashed line) and density (solid black line) of the trajectory used for the ^{13}C-pocket in this study.

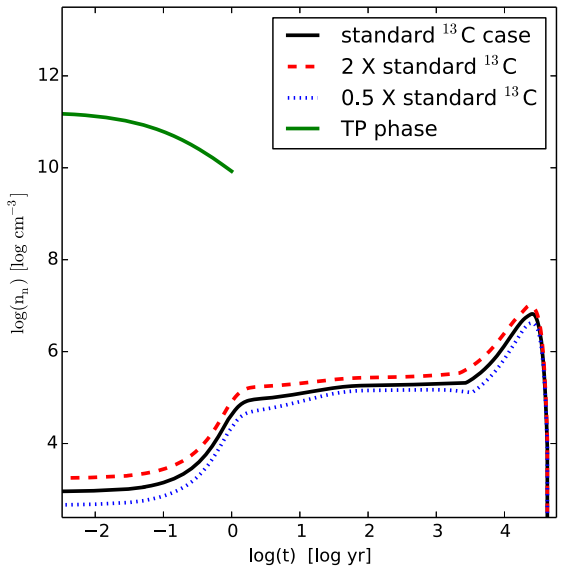

Figure 2. Time evolution of the neutron density (cm^{-3}) for the three initial ^{13}C abundances considered in the ^{13}C-pocket and the TP phase.

variations in the initial content of ^{13}C that lead to an s-process production similar to the one predicted by full stellar models. Our tests revealed that an initial mass fraction of ^{13}C of $X_{^{13}C} = 1.95 \times 10^{-2}$ enables us to produce a typical s-process pattern with the above trajectory. We call our calculations using this value of ^{13}C our 'standard' case. To fully explore the range of conditions found in low-mass stars, we also used two additional initial ^{13}C abundances, one in which the standard initial abundance of ^{13}C is halved ('0.5 × ^{13}C' case), whereas in the other one it is doubled ('2 × ^{13}C' case). The variations in the neutron densities for the three cases are shown in Fig. 2. The initial composition for our calculations is given in Table 1 for nuclides for which we do not use the standard solar composition. Besides the change in ^{13}C explained above, the other initial abundances for our calculations were extracted from the same stellar evolution model as the trajectory.

Table 1. Initial composition for the nuclei that differ from the solar composition during the ^{13}C-pocket.

Nuclei	Mass fraction	Nuclei	Mass fraction
^{1}H	1.08×10^{-29}	^{16}O	4.32×10^{-2}
^{2}H	1.43×10^{-5}	^{17}O	2.80×10^{-6}
^{3}He	4.49×10^{-5}	^{18}O	4.83×10^{-8}
^{4}He	4.58×10^{-1}	^{19}F	1.79×10^{-9}
^{6}Li	6.44×10^{-10}	^{20}Ne	1.23×10^{-3}
^{7}Li	9.15×10^{-9}	^{21}Ne	3.09×10^{-6}
^{9}Be	1.68×10^{-10}	^{22}Ne	3.12×10^{-2}
^{10}B	7.75×10^{-10}	^{23}Na	3.10×10^{-5}
^{11}B	3.43×10^{-9}	^{24}Mg	5.86×10^{-4}
^{12}C	3.31×10^{-1}	^{25}Mg	7.73×10^{-5}
^{13}C	1.95×10^{-2}	^{26}Mg	8.86×10^{-5}
^{14}N	5.11×10^{-3}	^{27}Al	5.91×10^{-5}
^{15}N	9.02×10^{-8}	^{28}Si	6.49×10^{-4}

Table 2. Initial composition for the light nuclei during the TP phase.

Nuclei	Mass fraction	Nuclei	Mass fraction
^{1}H	5.35×10^{-23}	^{16}O	6.00×10^{-3}
^{2}H	1.37×10^{-5}	^{17}O	1.00×10^{-10}
^{3}He	4.29×10^{-5}	^{18}O	1.00×10^{-10}
^{4}He	7.91×10^{-1}	^{19}F	1.5×10^{-5}
^{6}Li	6.44×10^{-10}	^{20}Ne	7.00×10^{-4}
^{7}Li	8.75×10^{-9}	^{21}Ne	1.00×10^{-5}
^{9}Be	1.68×10^{-10}	^{22}Ne	1.50×10^{-2}
^{10}B	7.41×10^{-10}	^{23}Na	1.80×10^{-4}
^{11}B	3.28×10^{-9}	^{24}Mg	7.00×10^{-4}
^{12}C	1.75×10^{-1}	^{25}Mg	7.00×10^{-5}
^{13}C	1.50×10^{-7}	^{26}Mg	1.00×10^{-4}
^{14}N	5.00×10^{-3}	^{27}Al	7.00×10^{-5}
^{15}N	5.00×10^{-6}	^{28}Si	5.00×10^{-4}

Besides the ^{13}C-pocket, neutron captures also take place at the bottom of the TP-driven convective zone (PDCZ) as explained in the introduction. In low-mass AGB stars ($M < 4$ M$_\odot$, which dominate the overall s-process production given to the initial mass function), only a small production of neutron-rich isotopes is expected from the TP phase, such as ^{96}Zr (otherwise not produced during the radiative burning of the ^{13}C-pocket). Given that the TP only contributes a short neutron burst and has a very small contribution to the overall s-process production, we approximated the TP conditions with a single-zone trajectory as in Ko16. The trajectory lasts for 1 yr, with a constant temperature of 0.245 GK and a constant density of 5 × 10^3 g cm^{-3}. The initial abundances are summarized in Table 2 for light elements; for the other elements, the final abundances of the standard ^{13}C-pocket were diluted by a factor of 20 to take into account the diluting effect of the PDCZ. The chosen trajectory, combined with the initial composition described above, is able to roughly reproduce typical isotopic compositions obtained during TP by more complex stellar evolution codes (Cristallo et al. 2015). The time evolution of the neutron density for the TP phase is also shown in Fig. 2.

2.1.1 *Comparison to the Cristallo et al. (2011) yields*

To validate our trajectory and initial composition combination, we compared the final abundances of our calculations at solar

metallicity to the s-process pattern determined using full stellar models by Cristallo et al. (2011) (C11 hereinafter, but see also for details Straniero et al. 2006; Cristallo et al. 2009, 2007) for stars of 1.5, 2, and 3 $M_\odot$ at solar metallicity. Our calculations used a single trajectory covering a single 13C-pocket whereas the C11 computed full stellar models. The s-process produced in the ^{13}C-pocket in their models is thus diluted into the convective envelope following the TDU. We thus used a dilution factor f to compare our final abundance to theirs. We set the dilution factor f to match the production of ^{88}Sr in our computations to the production in the 2 $M_\odot$ model of C11:

$$\frac{f\,{}^{88}\mathrm{Sr}\,Y_{\mathrm{out}}^{\mathrm{traj}} + (1-f)\,{}^{88}\mathrm{Sr}\,Y_{\mathrm{ini}}^{traj}}{{}^{88}\mathrm{Sr}\,Y_{\mathrm{ini}}^{\mathrm{traj}}} = \frac{{}^{88}\mathrm{Sr}\,Y_{\mathrm{out}}^{\mathrm{C11}}}{{}^{88}\mathrm{Sr}\,Y_{\mathrm{ini}}^{\mathrm{C11}}} \quad (1)$$

where ${}^{88}\mathrm{Sr}\,Y_{\mathrm{ini}}^{\mathrm{traj}}$ is the initial abundance of Sr in our trajectory, ${}^{88}\mathrm{Sr}\,Y_{\mathrm{out}}^{\mathrm{traj}}$ is the final abundance (same for the C11 production factors). Our final diluted abundances are compared to the C11 production factors in Figs 3, 4, 5, and 6.

The good overall agreement between our standard model and the C11 yields shows that our trajectory is adequate to determine the key nuclear reactions that strongly affect s-process predictions. Nevertheless, it is also clear that a single trajectory – as the one we adopt – is not able to reproduce the full range of conditions occurring in low-mass stars. We thus added to our investigations two other initial abundances for ^{13}C, with the aim of covering a wider range of conditions of the s-process. It also allows us to determine the sensitivity of our results to the thermodynamic conditions and neutron flux in particular. Furthermore, since the main difference between models of main s-process production is the ratio between seed (given by the metallicity, mainly iron) and the neutrons (given by the ^{13}C present at the start of the calculation) we are also investigating in some respect the metallicity dependence of this process. For the purpose of determining key rates, it is not necessary to match exactly the final results of Cristallo et al. (2011). More important is to investigate the full range of neutron fluxes and the activated branches. Figs 3, 4, 5, and 6 show that – excluding rare cases – the results we obtain with the three initial ^{13}C contents cover the full range of results obtained by C11 and thus prove that our approach is suitable to determine the uncertain key rates for the s-process in low-mass stars. It is more difficult to apply a similar approach in the case of the TP phase. This is because the overall production during the TP is tiny compared to that occurring during the ^{13}C-pocket. Therefore, there is no way to directly compare the output from this phase and the final theoretical results. We show in Fig. 7 the production factors of all the considered nuclei. There is significant production of only a few isotopes, and of these, most are not produced by our ^{13}C trajectory (see Figs 3–6). These neutron-rich isotopes are in fact expected to mainly be produced during the TP phase in AGB stars (Gallino et al. 1998).

2.2 MC procedure

The thermodynamic trajectory described above was post-processed using the PizBuin code suite. This suite consists of a fast reaction network and a parallelized MC driver. We followed the same procedure as presented in detail in Rauscher et al. (2016). The nucleosynthesis calculation was repeated 10 000 times, with different rate variation factors each time, and the combined output was analysed subsequently. The simultaneous variation of rates is superior to a decoupled variation of individual rates as performed in the past and in Ko16 because neglecting a combined change in rates may lead to an overemphasis of certain reactions and an overestimation of their impact on the total uncertainty (Rauscher et al. 2016; Rauscher et al. 2017).

In our method, we define key rates to be those dominating the uncertainty of a given final abundance. By this definition, reducing the uncertainty of a key rate will also considerably decrease the uncertainty in the final abundance of a given nuclide. The identification of key rates is obtained by examining the correlation between a change in a reaction rate and the change of an abundance. We used the Pearson product moment correlation coefficient to quantify these correlations. Positive values of the Pearson coefficients, r, indicate a positive correlation between rate change and abundance change, whereas negative values signify an inverse correlation, i.e. the abundance decreases when the rate is increased. The larger the absolute value of the Pearson coefficient, the stronger the correlation. As in Rauscher et al. (2016), Nishimura et al. (2017), and Nishimura et al. (2018), a level 1 key rate is identified by $r \geq 0.65$. Each astrophysical reaction rate involving elements from Fe to Bi was varied within its own uncertainty range. We used the same variation factor for forward and reverse rates as they are connected by detailed balance. The uncertainty range used is temperature dependent and constructed from a combination of the experimental uncertainty (if the rate has been measured) for target nuclei in their ground states and a theoretical uncertainty for predicted rates on nuclei in thermally excited states. Theory uncertainties were different depending on the reaction type and can be asymmetric. The reaction network consisted of 943 isotopes including all reactions relevant to the s-process, i.e. fusion reactions of lighter nuclei as well as (n,γ) reactions, electron captures, and β decays for heavier nuclei. The standard rate set and uncertainties used in this study are the same as in Rauscher et al. (2016) and Nishimura et al. (2017). Rates for neutron-, proton-, and α-induced reactions were a combination of theoretical values by Rauscher & Thielemann (2000) supplemented by experimental rates taken from Dillmann et al. (2006) and Cyburt et al. (2010); decays and electron captures were taken from a REACLIB file compiled by Freiburghaus & Rauscher (1999) and supplemented by rates from Takahashi & Yokoi (1987) and Goriely (1999) as provided by Aikawa et al. (2005) and Xu et al. (2013).

2.2.1 *Nuclide selection for the key rate determination*

Almost all the stable nuclides up to ^{209}Bi have an s-process contribution. We might therefore present key rates for almost 250 isotopes. If an isotope, however, constitutes a negligible fraction of the total elemental abundance, improving its key reaction rates would not make a difference to the total production of an element. We thus had to establish a selection procedure for nuclides to be presented in our key rate determination. One possible selection method is to consider a threshold in the production factors. This method failed because it was not possible to determine a suitable threshold; either too few or too many nuclides were excluded and the resulting exclusions were rather random. Concerning the analysis of the ^{13}C-pocket phase, we therefore decided to analyse only isotopes that contribute at least 10 per cent to the final total mass of the element. This selection method yields a list of 109 nuclides, most of which are listed in the tables below (note that only nuclides with a key rate are listed). In addition, we considered seven more nuclides ^{86}Sr, ^{87}Sr, ^{110}Cd, ^{123}Te, ^{134}Ba, ^{148}Sm, and ^{176}Hf. Although their total production factor is below the 10 per cent threshold explained above, they are s-only nuclides and are thus worth investigating. Regarding the analysis of the TP phase, a similar procedure

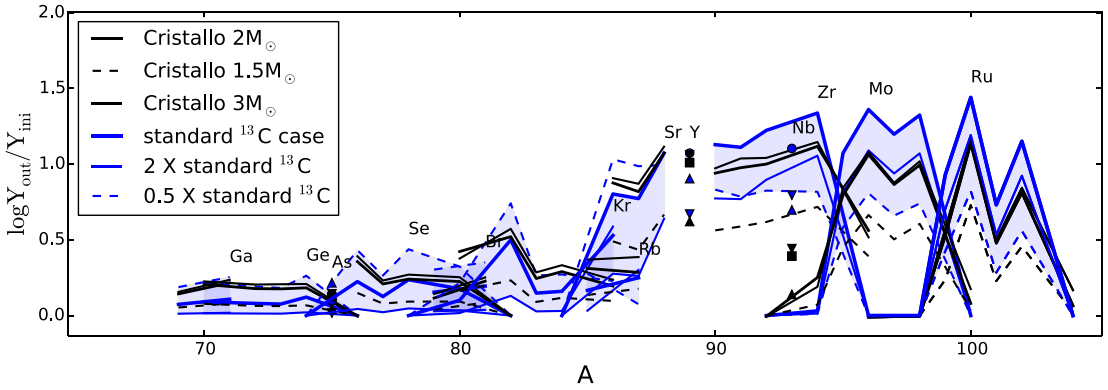

Figure 3. Production factors as a function of the atomic mass for elements from Ga to Ru during the ^{13}C-pocket. Comparison between the results obtained for a 1.5 (dashed black line – black triangle for monoisotopic elements), 2 (thick solid black line – black square), and 3 $M_{\odot}$ (thin solid black line – upside down black triangle) by C11 and the trajectory considered in this study with the three different initial abundances for ^{13}C: standard case (thick solid blue line – blue dot), half (dashed blue line – blue triangle), and double (thin solid blue line – upside down blue triangle) the standard case. The blue area highlights the range of s-process production obtained using the three cases for the initial ^{13}C abundance. Note that we applied a dilution factor, *f*, to our results to compare them to production factors of C11 (see equation 2.1.1).

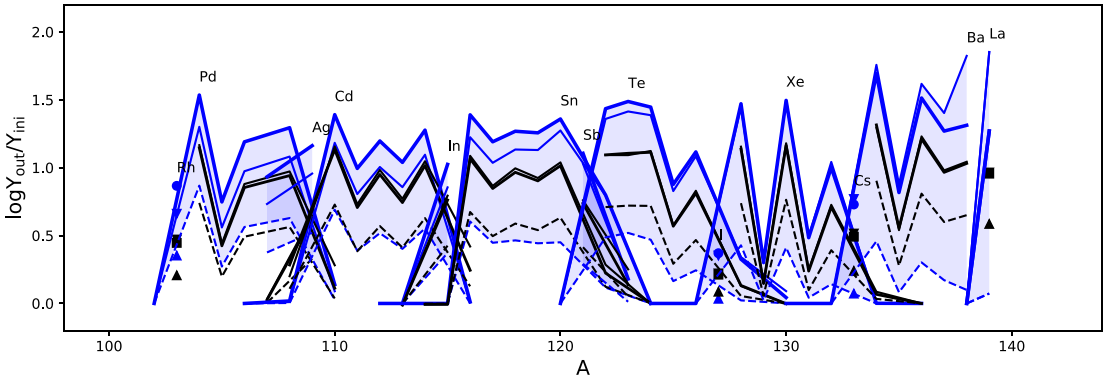

Figure 4. Same as Fig. 3 for elements from Rh to La.

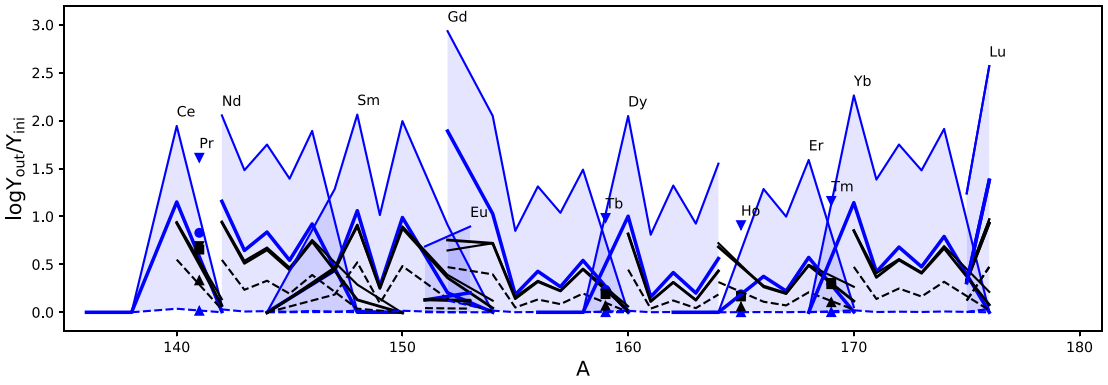

Figure 5. Same as Fig. 3 for elements from Ce to Lu.

fails to select all the isotopes that characterized this production; we therefore select all the isotopes not destroyed whose production is above 1 per cent of their production during the ^{13}C-pocket phase. In this way, we exclude isotopes that have negligible production during the TP phase. To the isotopes selected in this way, we have added the s-only nuclides and the final list contains 58 nuclei (see Table 4).

3 RESULTS AND DISCUSSION

As explained above, we used the PizBuin code suite to determine the uncertainty in the final s-process abundances due to uncertainties of reactions involving heavy elements as well as the key reactions dominating these uncertainties. The total uncertainties of the final abundances are given in Table 3 for the ^{13}C-pocket and in Table 4 for the TP phase and shown in Figs 8 and 9, respectively.

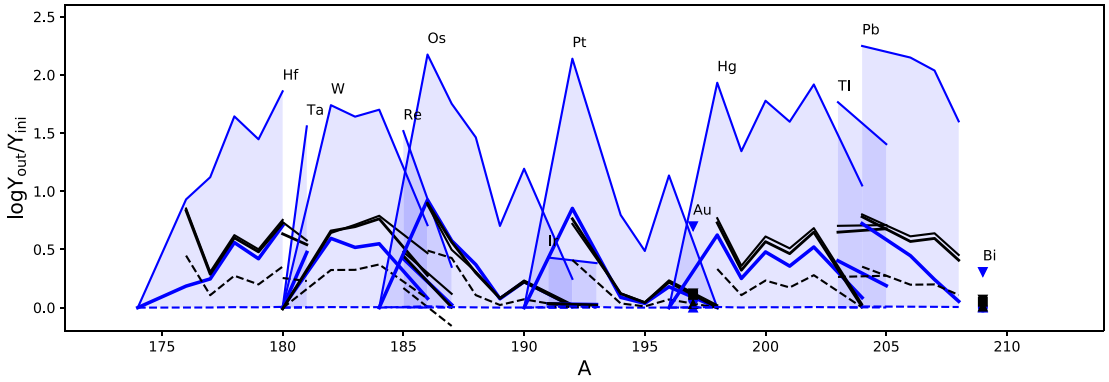

Figure 6. Same as Fig. 3 for elements from Hf to Bi.

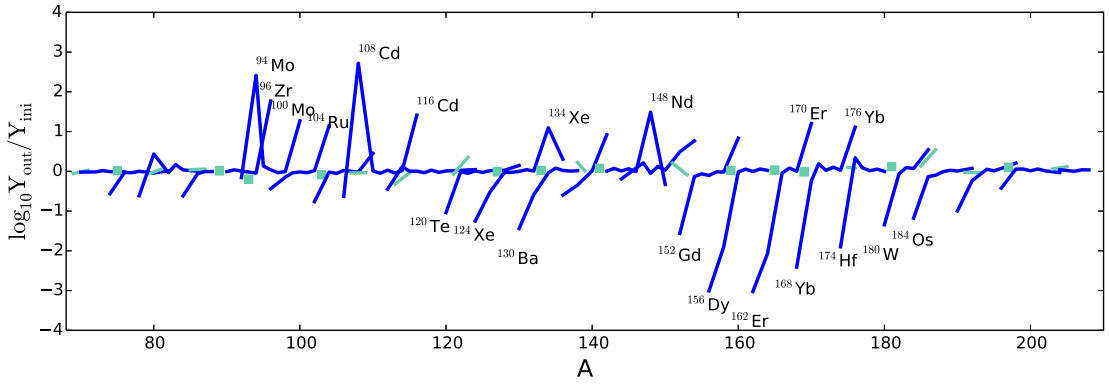

Figure 7. Production factors (final abundances divided by the initial abundances used for the TP trajectory) as a function of the atomic mass for elements from Ga to Pb during the TP phase. The blue lines connect elements with even atomic number, other elements are presented in cyan. Isotopes with a production factor greater than 10 or less than 0.1 are indicated.

3.1 Total uncertainties

As can be seen in Table 3 and Fig. 8, the overall uncertainties during the ^{13}C-pocket are generally small. Indeed, most of them are smaller than 50 per cent. This is not too surprising since the relevant temperature range (∼8 keV) is accessible to experimental measurements for many of the relevant rates, which are along the valley of stability, have already been measured experimentally. Furthermore, excited states generally have a weak contribution in this temperature range so the nuclear uncertainties are generally small to start with. There are nevertheless several nuclides, for which uncertainties are larger than a factor of 2. These are generally nuclides around branching points such as ^{86}Kr. We also notice a propagation effect for nuclides more massive than ^{138}Ba. This is due to the combined effect of uncertainties in neutron-capture rates above ^{138}Ba. For the TP case, we find somewhat larger uncertainties (see Table 4 and Fig. 9), in several cases greater than a factor of 2, and in four cases reaching a factor of 3. This is both due to the higher temperatures encountered, and the effect that at branching points there is a stronger sensitivity to the ratio between beta-decay rates and capture rates.

3.2 Key rates

As explained in Section 2.2, key rates are obtained by examining the correlation between a change in a reaction rate and the change of an abundance. The key reaction rates are listed in Table A1 for levels 1, 2, and 3 (for an explanation of key rate levels, see Section 3.2.1). Most of them are neutron-capture reactions either directly producing or destroying the nuclide in question. This is not surprising because steady-flow equilibrium applies to most of the s-process path between the peaks. We nevertheless list all of them in the Appendix for completeness. Moreover, not all of the selected isotopes and key reactions appear at same level or with the same correlation, thus indicating the impact of specific reactions, or the impact of different degrees of constraint in experimental uncertainty on final abundances. Notable exceptions for the ^{13}C-pocket are neutron captures on ^{56}Fe, ^{64}Ni, and ^{138}Ba, which are level 2 key rates for many nuclides. We will come back to these three reactions in Section 3.4.1. There are also a few key weak reactions at branching points, ^{79}Se, ^{85}Kr, and ^{128}I. We will discuss the possibility of reducing the uncertainties of the key reactions linked to the most uncertain final abundances in Section 3.6. For the TP phase, there are two exceptions, the neutron-capture reactions ^{56,57}Fe(n, γ). While this may be surprising at first, ^{56,57}Fe act as 'poisons' in the TP phase. Indeed, they compete for neutrons with heavier nuclides and the neutron burst in the TP phase is too short for iron to act as a seed for the heavy elements produced during the TP.

3.2.1 *Uncertainties for the different key reaction levels*

As in our previous studies, we determined level 2 key reactions by using the standard rates for all previously identified (level 1) key reaction rates and performing another MC variation without varying those rates. This shows the effect when the level 1 key rates would have been determined. Level 2 key rates are then key

Table 3. Uncertainties in the final abundance of s-process nuclides from the MC calculation for the standard ^{13}C-pocket phase. The column labelled 'Level' indicates the level of the first key reaction found. The remaining columns show uncertainty factors for variations Up and Down, the values of which are Y(95 per cent)/Y_{peak} and Y(5 per cent)/Y_{peak}, respectively. They enclose a 90 per cent probability interval, as shown in Fig. 8.

Nuclide	Level	Up	Down	Nuclide	Level	Up	Down
^{69}Ga	1	1.13	0.896	^{138}Ba	2	1.08	0.941
^{71}Ga	1	1.24	0.918	^{139}La	1	1.34	0.922
^{70}Ge	1	1.18	0.888	^{140}Ce	2	1.12	0.877
^{72}Ge	1	3.23	0.944	^{141}Pr	2	1.09	0.854
^{74}Ge	1	1.51	0.966	^{142}Nd	3	1.17	0.886
^{75}As	1	1.14	0.936	^{144}Nd	–	1.14	0.860
^{76}Se	1	1.17	0.939	^{146}Nd	3	1.17	0.880
^{78}Se	1	1.98	0.971	^{147}Sm	3	1.14	0.858
^{80}Se	1	1.29	0.939	^{148}Sm	3	1.19	0.889
^{79}Br	1	2.79	0.962	^{150}Sm	3	1.17	0.878
^{81}Br	1	1.08	0.942	^{151}Eu	1	1.23	0.810
^{80}Kr	1	2.57	0.782	^{153}Eu	–	1.14	0.842
^{82}Kr	1	1.25	0.940	^{152}Gd	3	1.18	0.768
^{84}Kr	1	1.52	0.970	^{154}Gd	3	1.15	0.854
^{86}Kr	1	1.78	0.472	^{156}Gd	3	1.15	0.852
^{85}Rb	1	1.07	0.943	^{158}Gd	–	1.15	0.848
^{87}Rb	1	1.94	0.514	^{159}Tb	1	1.37	0.833
^{86}Sr	1	1.17	0.945	^{160}Dy	–	1.20	0.878
^{87}Sr	1	1.15	0.957	^{162}Dy	–	1.17	0.855
^{88}Sr	1	1.06	0.950	^{164}Dy	3	1.20	0.861
^{89}Y	1	1.10	0.926	^{165}Ho	1	1.29	0.844
^{90}Zr	1	1.12	0.907	^{166}Er	1	1.40	0.818
^{92}Zr	1	1.21	0.932	^{167}Er	1	1.39	0.846
^{94}Zr	1	1.13	0.923	^{168}Er	1	1.57	0.826
^{93}Nb	1	1.46	0.945	^{169}Tm	1	1.76	0.806
^{95}Mo	1	1.13	0.927	^{170}Yb	–	1.21	0.873
^{96}Mo	1	1.32	0.967	^{172}Yb	–	1.17	0.836
^{97}Mo	1	1.12	0.910	^{174}Yb	–	1.19	0.847
^{98}Mo	1	1.26	0.927	^{175}Lu	3	1.21	0.871
^{99}Ru	1	1.20	0.943	^{176}Lu	3	1.19	0.848
^{100}Ru	1	1.19	0.908	^{176}Hf	3	1.27	0.833
^{102}Ru	1	1.13	0.926	^{178}Hf	–	1.22	0.866
^{103}Rh	1	1.28	0.939	^{180}Hf	–	1.19	0.841
^{104}Pd	1	1.46	0.968	^{181}Ta	1	1.52	0.788
^{106}Pd	1	1.42	0.943	^{182}W	–	1.20	0.837
^{108}Pd	1	1.37	0.918	^{183}W	3	1.20	0.800
^{107}Ag	1	1.11	0.936	^{184}W	–	1.23	0.859
^{109}Ag	1	1.08	0.914	^{185}Re	–	1.19	0.820
^{110}Cd	2	1.05	0.939	^{186}Os	–	1.25	0.852
^{112}Cd	2	1.06	0.952	^{187}Os	1	1.72	0.820
^{114}Cd	2	1.06	0.953	^{188}Os	3	1.22	0.825
^{115}In	1	1.39	0.912	^{190}Os	–	1.22	0.827
^{116}Sn	1	1.05	0.938	^{191}Ir	–	1.20	0.820
^{118}Sn	2	1.07	0.948	^{193}Ir	3	1.31	0.815
^{120}Sn	2	1.06	0.953	^{192}Pt	1	2.31	0.871
^{121}Sb	1	1.19	0.954	^{194}Pt	1	2.91	0.850
^{122}Te	–	1.06	0.957	^{196}Pt	3	1.32	0.795
^{123}Te	–	1.04	0.945	^{197}Au	–	1.24	0.838
^{124}Te	3	1.06	0.955	^{198}Hg	2	1.31	0.782
^{126}Te	1	1.07	0.950	^{200}Hg	1	1.36	0.774
^{127}I	1	1.16	0.945	^{202}Hg	–	1.34	0.858
^{128}Xe	1	1.04	0.908	^{203}Tl	3	1.30	0.779
^{130}Xe	2	1.06	0.958	^{205}Tl	1	2.40	0.772
^{132}Xe	1	1.33	0.957	^{204}Pb	–	1.27	0.797
^{133}Cs	1	1.13	0.949	^{206}Pb	–	1.30	0.763
^{134}Ba	1	1.08	0.935	^{207}Pb	–	1.43	0.792
^{136}Ba	1	1.12	0.954	^{208}Pb	–	1.39	0.784
^{137}Ba	1	1.09	0.950	^{209}Bi	3	1.38	0.746

Table 4. Uncertainties in the final abundance of s-process nuclides from the MC calculation for the TP phase. The column labelled 'Level' indicates the level of the first key reaction found. The remaining columns show uncertainty factors for variations Up and Down, the values of which are Y(95 per cent)/Y_{peak} and Y(5 per cent)/Y_{peak}, respectively. They enclose a 90 per cent probability interval, as shown in Fig. 9.

Nuclide	Level	Up	Down	Nuclide	Level	Up	Down
^{70}Ge	1	1.04	0.946	^{134}Ba	2	1.08	0.923
^{76}Se	1	1.06	0.901	^{136}Ba	1	1.03	0.988
^{82}Se	1	1.14	0.941	^{138}La	1	2.56	0.919
^{80}Kr	1	1.11	0.789	^{142}Ce	1	3.42	0.619
^{86}Sr	1	1.04	0.977	^{142}Nd	–	1.01	0.974
^{87}Sr	1	1.05	0.960	^{148}Nd	1	2.09	0.442
^{96}Zr	1	3.73	0.469	^{148}Sm	2	1.10	0.862
^{94}Mo	1	1.21	0.879	^{150}Sm	1	1.11	0.956
^{96}Mo	1	1.08	0.900	^{152}Sm	1	1.10	0.918
^{100}Mo	1	1.73	0.466	^{154}Sm	–	3.40	0.602
^{100}Ru	1	1.11	0.912	^{152}Gd	1	1.41	0.263
^{104}Ru	1	1.81	0.456	^{154}Gd	1	1.16	0.886
^{104}Pd	1	1.31	0.956	^{160}Gd	1	2.14	0.500
^{110}Pd	1	1.39	0.388	^{160}Dy	1	1.29	0.884
^{108}Cd	–	1.11	0.926	^{170}Er	1	3.52	0.627
^{110}Cd	1	1.06	0.927	^{170}Yb	1	1.94	0.727
^{116}Cd	1	1.39	0.256	^{176}Yb	1	1.34	0.414
^{114}Sn	1	1.04	0.928	^{176}Lu	1	1.12	0.867
^{115}Sn	1	1.05	0.923	^{186}W	1	2.14	0.878
^{116}Sn	1	1.02	0.970	^{187}Re	3	1.85	0.843
^{124}Sn	1	1.07	0.783	^{186}Os	1	1.20	0.674
^{122}Te	1	1.04	0.944	^{187}Os	1	2.13	0.762
^{123}Te	2	1.06	0.932	^{192}Os	1	1.28	0.680
^{124}Te	1	1.01	0.973	^{192}Pt	1	1.92	0.686
^{130}Te	1	1.40	0.927	^{195}Pt	1	2.96	0.841
^{128}Xe	1	1.04	0.883	^{198}Pt	1	1.39	0.448
^{130}Xe	1	1.02	0.961	^{198}Hg	1	1.13	0.890
^{134}Xe	1	2.38	0.639	^{204}Pb	1	1.04	0.951
^{136}Xe	1	2.06	0.835	^{209}Bi	1	1.02	0.996

to the remaining uncertainties. Similarly, level 3 key rates were determined by exempting level 1 *and* level 2 key rates from the MC variation. It has to be emphasized that level 2 and level 3 key reactions are only important *provided that level 1 and level 2 rates, respectively, have been constrained*.

Figs 10 and 11 show the total uncertainties obtained for levels 2 and 3, respectively. We see that already at level 2, uncertainties are tiny for nuclides lighter than ^{138}Ba. Exceptions are a few isotopes at branching points (^{80}Kr, ^{86}Kr, and ^{87}Rb). The propagation effect for nuclides more massive than ^{138}Ba remains. The total uncertainty has already significantly decreased compared to level 1 so limited improvements can be made by future measurements of the level 2 rates. The level 3 uncertainties shown in Fig. 11 show that all key rates were identified at level 1 or 2 and that the uncertainties are negligible once these have been determined. The same is true for the TP phase.

3.3 Dependence of uncertainties and key rates on astrophysical conditions

We used a single-zone trajectory to mimic the astrophysical conditions taking place in the TP-AGB phase of low-mass stars in our MC calculations. A single-zone trajectory cannot capture the full conditions found in stars. As explained in Section 1, conditions vary in stars and there are still major uncertainties in the modelling of the TP-AGB phase and in particular concerning the formation

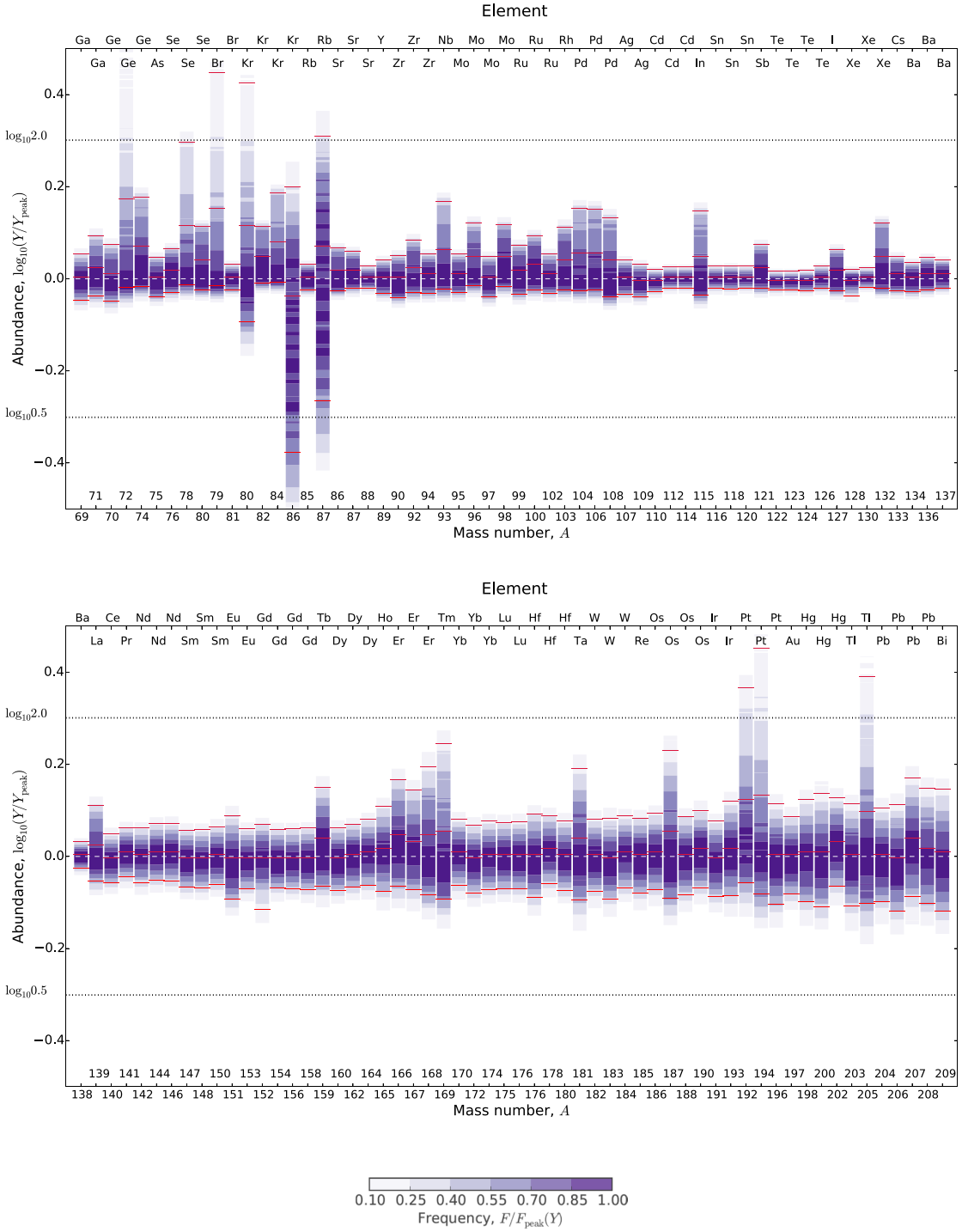

Figure 8. Total production uncertainties in the final s-process abundances obtained with the trajectory described in the previous section for the ^{13}C-pocket with the standard initial abundance. The colour shading denotes the probabilistic frequency and the 90 per cent probability intervals up and down are marked for each nuclide with the red lines. The final abundances are normalized by the final abundance at the peak of the distribution. Horizontal dotted lines indicate a factor of 2 uncertainties.

of the ^{13}C-pocket. Nevertheless, as our comparison to the yields of C11 in Section 2.1.1 shows, using an initial ^{13}C abundance divided ('0.5 × ^{13}C' case) and multiplied ('2 × ^{13}C' case) by a factor of 2 compared to the standard case samples the variations in the s-process production in stars of different masses. It also samples different neutron-to-seed ratios and thus to some extent the metallicity dependence of our results. More generally, it allows us to determine the sensitivity of our results to the astrophysical conditions found in the ^{13}C-pocket. Figs 3, 4, 5, and 6 show that in the '0.5 × ^{13}C' case, the production stops around ^{138}Ba and therefore that this case underestimates the neutron flux needed to produce the main s-process. This leads to a stronger production for elements between iron and strontium. In the '2 × ^{13}C' case, the production is very strong all the way up to lead with overproduction factors much

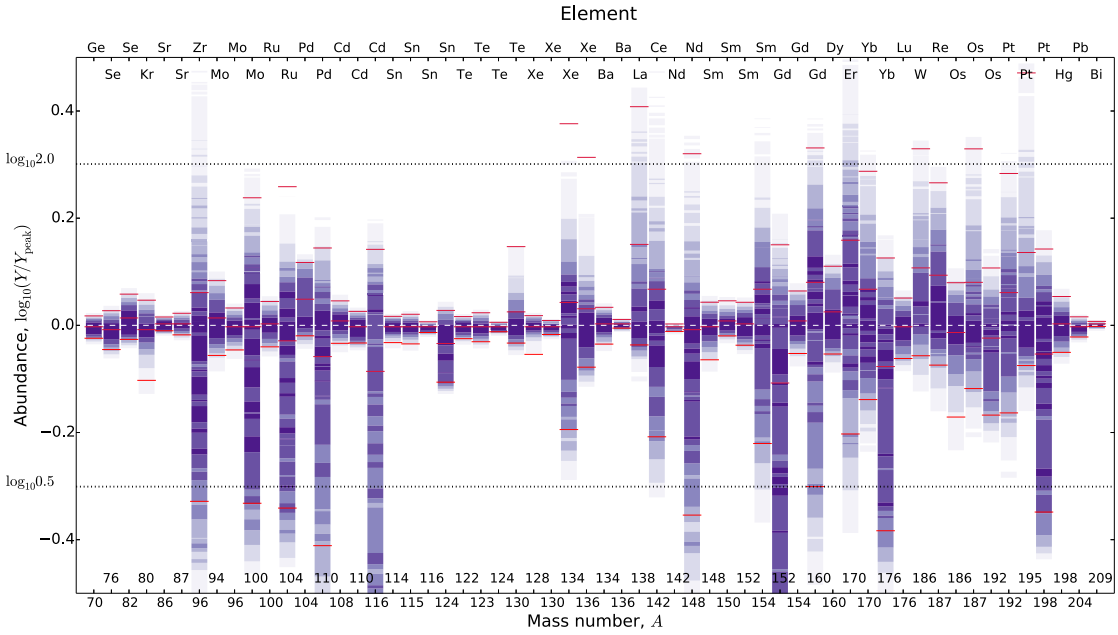

Figure 9. Total production uncertainties in the final s-process abundances obtained with the trajectory described in the previous section for the TP phase. The colour shading denotes the probabilistic frequency and the 90 per cent probability intervals up and down are marked for each nuclide with the red lines. The final abundances are normalized by the final abundance at the peak of the distribution. Horizontal dotted lines indicate a factor of 2 uncertainties.

larger than those of C11. This means that the neutron flux in this case is very strong and the elements between iron and strontium are depleted. We thus do not consider the two additional cases as representative cases for the main s-process. This is why we do not list the total uncertainties for these two cases in tables. Rather we use them to test the robustness of the key rates list against variations that are larger than the variations expected to occur in real stars.

The total uncertainties for the two additional cases are shown in Figs 12 and 13. Comparing these figures to Fig. 8 for the standard case, we see that the same nuclides have the largest uncertainties. We also see that uncertainties are generally small (less than 50 per cent) for most nuclides in the three cases. The main difference between the three cases is the extent of the propagation effects. Since the flow stops around barium for the '0.5 × ^{13}C' case, the propagation effect is strongest in this case for elements around and above barium. In the '2 × ^{13}C' case, propagation effects are very small because the production easily reaches lead.

We list the key rates for the three cases in Tables A1, A2, andA3 in the Appendix. Comparing Table A2 to Table A1, we see that all but one key rates for the '0.5 × ^{13}C' case were already key rates for the standard case. The exception is ^{209}Bi(n, γ)^{210}Bi, which is not important in this particular case because there is no production beyond barium. Comparing Table A3 to Table A1, we see again that most key rates for the '2 × ^{13}C' case were already key rates for the standard case. The very strong flux in the '2 × ^{13}C' case leads to a production, which follows a slightly more neutron-rich path and thus to a few more key rates that were not present in the standard case. The strong overlap in the key reaction lists between the standard case and the other two cases representing a very weak and very strong neutron flux shows that our reference key reaction list is a representative of the full range of astrophysical conditions found in the ^{13}C-pocket.

3.4 Comparison to past sensitivity studies

The key differences between the approach used in this study and past studies are explained in Rauscher et al. (2017) and Rauscher et al. (2016). We summarize them here:

(i) Instead of varying rates one-by-one, all rates involving heavy elements in the network are varied simultaneously in an MC framework.

(ii) Key reactions are identified by inspection of correlations in the simultaneous variation of all rates instead of relying on the sensitivity of an abundance to the individual variation of a single rate.

(iii) Each rate is assigned an individual uncertainty which is temperature dependent and which is sampled by a different MC variation factor for each rate. Uncertainties do not have to be symmetric.

(iv) The bespoke rate uncertainties are derived and are based on both experimental data for the ground-state contributions when available and a theoretical uncertainty for the excited-states contributions.

Varying rates one-by-one may result in an incorrect assessment of total uncertainties as well as the importance of the selected rates. This is due to the fact that the combined action of several reactions can cover or enhance uncertainties in each single rate. We rather define a key reaction as a reaction dominating the uncertainty of the final abundance of a given nuclide. This means that this abundance uncertainty will be considerably reduced when better constraining the corresponding key reaction. Key reactions are specific to a nuclide and it is possible that no key reaction can be found for a given nuclide when many reactions are contributing to its abundance.

As explained in the Introduction, Koloczek et al. (2016) (Ko16) recently reviewed the impact on the main s-process of current nuclear uncertainties considering both the ^{13}C-pocket and TP conditions. Ko16 varied reaction rates one-by-one so it is interesting to compare our results to theirs. Note that this study focused on inter-

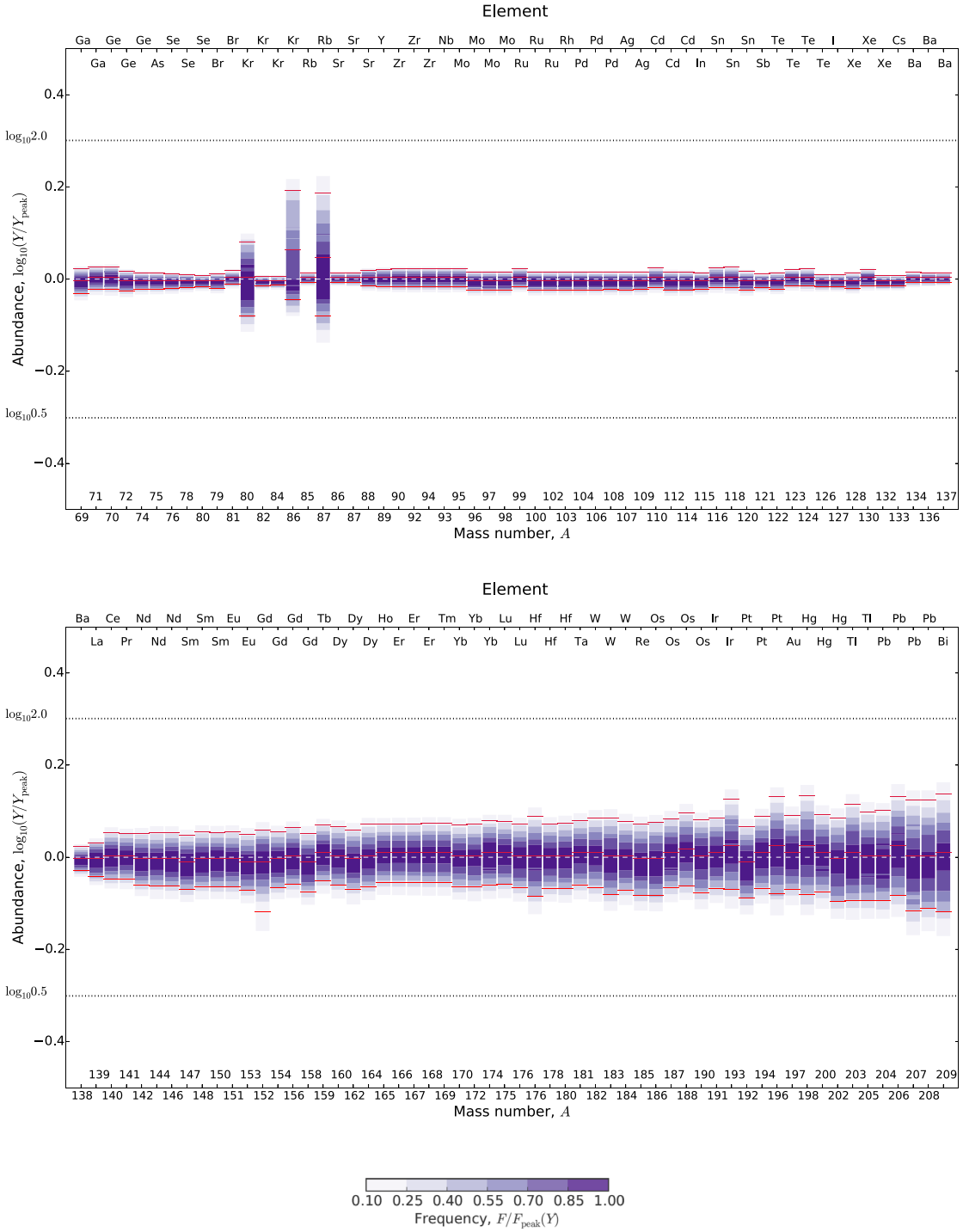

Figure 10. Same as Fig. 8 except that all the level 1 key reactions are now fixed to show the improvements that determining all level 1 rates would make.

mediate and heavy elements and therefore this is the atomic mass range that we will compare. The uncertainties for rates involving light elements are generally well established and we refer the reader to the Ko16 and Käppeler et al. (2011) studies (and references therein) concerning nuclear uncertainties linked to light elements (e.g. neutron sources and neutron poisons). Ko16 provide a list of the strongest globally affecting reactions during both the TP (their Table A) and the ^{13}C-pocket (their Table B), which is very valuable information. Since rates were varied individually, however, it is not clear whether or not the rates in question dominate the uncertainties for all the nuclides affected by that reaction. Re-measuring the rates listed in tables A and B of Ko16 may thus not reduce the uncertainties in predicted production of all the nuclides affected. Our definition of key rates gives exactly this information since a rate is only key if it dominates the uncertainty of a given nuclide. Our study shows that in many cases, the key rates dominating the nuclear uncertainties are the neutron captures either directly producing or destroying the nuclide in question. Nevertheless, all the

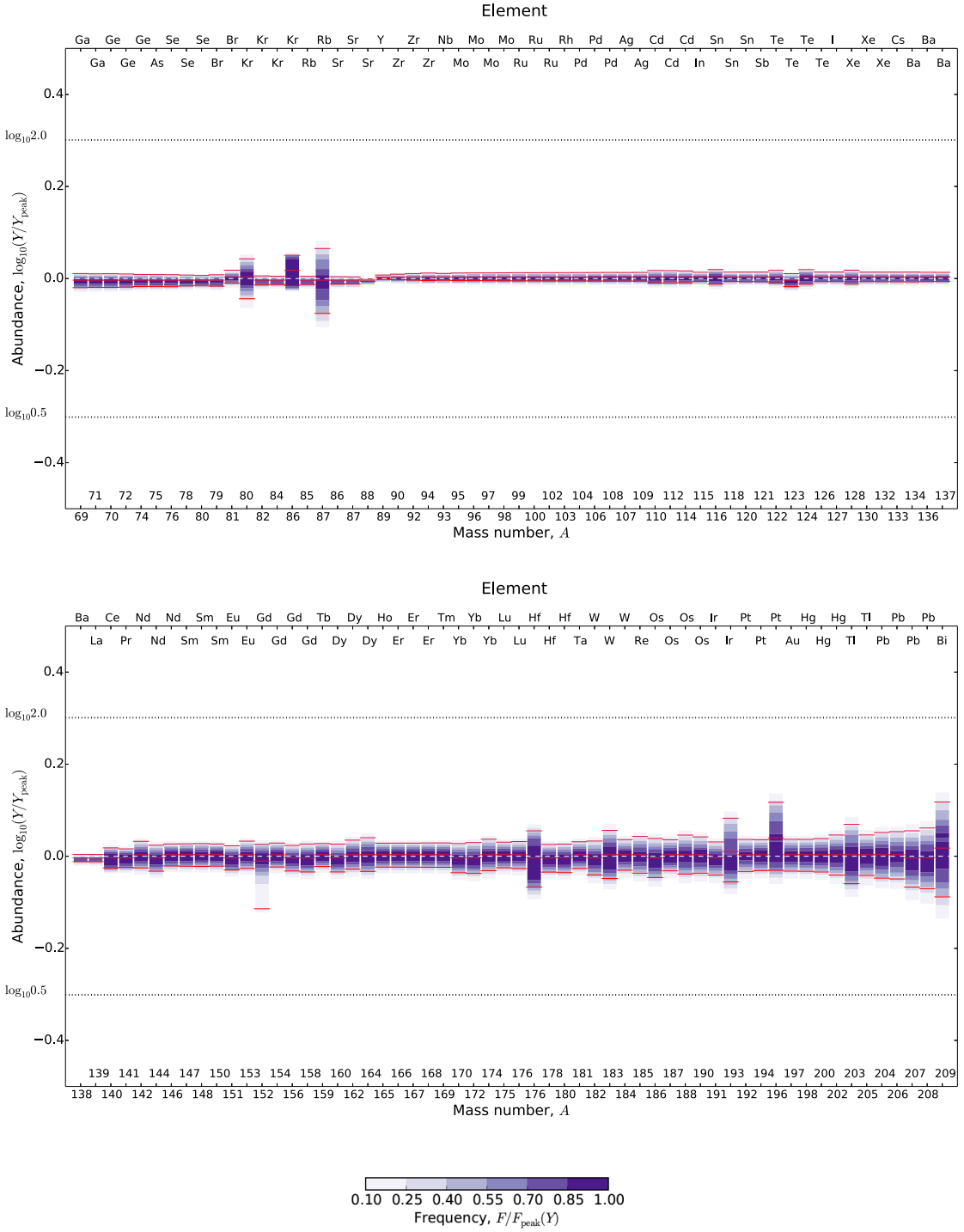

Figure 11. Same as Fig. 8 except that all the level 1 and 2 key reactions are now fixed.

rates involving heavy elements listed for the ^{13}C-pocket conditions by Ko16 (Table B) appear as key rates for at least one nuclide in our standard ^{13}C-pocket case. There are special rates, neutron captures on ^{56}Fe, ^{64}Ni, and ^{138}Ba, which we discuss below. We did not find in our TP phase the same reactions as found by Ko16 (cf. their table A). The different methodologies and the limited cases studied are likely responsible. Nevertheless, we note that most of the reactions found by Ko16 for the TP conditions are actually key rates for the standard case or the '2 $\times^{13}$C' case (which correspond to higher neutron densities compared to the standard ^{13}C-pocket case). The only significant rates we found in the TP condition, which are not either directly producing or destroying the nuclide in question (or very close by nuclei), are ^{57}Fe(n, γ) and ^{56}Fe(n, γ). These rates, however, only appear for one nuclide (148Nd) at level 2 so should be treated as any other level 2 key reactions (i.e. only be considered after all level 1 key rates have been improved). Finally, for the TP phase, we obtained several more β-decay reactions as key rates for the selected nuclei, compared to the ^{13}C-pocket conditions. How-

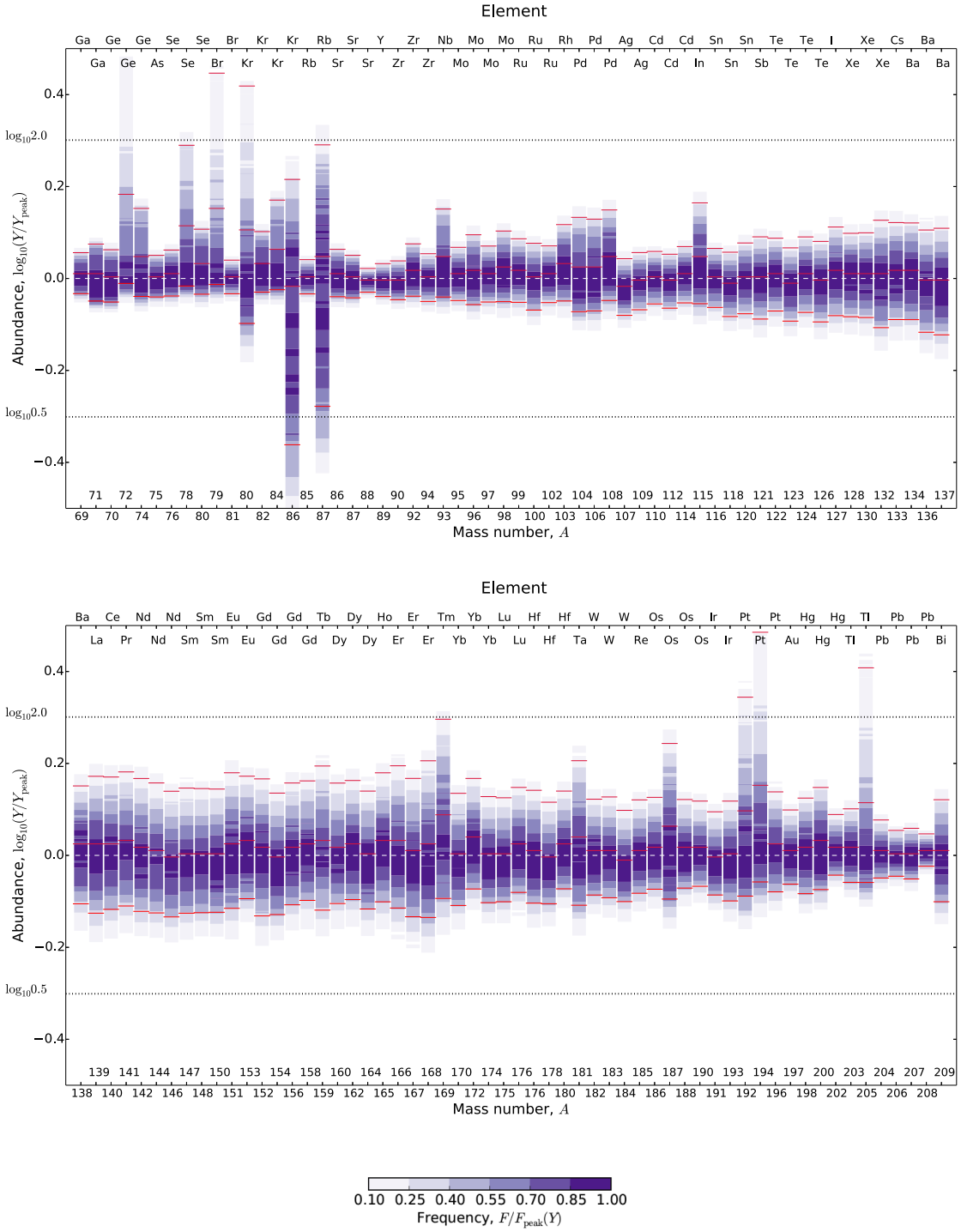

Figure 12. Total production uncertainties (same as Fig. 8) for the case with half of the standard initial ^{13}C abundance ('0.5 × ^{13}C ' case).

ever, as before, most of the uncertainty in the final abundances is caused by the uncertainty in the neutron-capture rates.

3.4.1 Neutron captures on ^{56}Fe, ^{64}Ni, and ^{138}Ba

As explained above, in most cases, key rates dominating the nuclear uncertainties are the neutron captures either directly producing or destroying the nuclide in question. There are, however, three neutron-capture rates that play a significant role in the uncertainty for many nuclides during the ^{13}C-pocket conditions. These are the neutron-capture rates on ^{56}Fe, ^{64}Ni, and ^{138}Ba. Neutron-capture rates on ^{56}Fe, ^{64}Ni, and ^{138}Ba appear as level 2 key rates for many nuclides in Table A1. This means that for many nuclides local neutron-capture rates are still the dominant source of uncertainty but the importance of these three neutron-capture rates becomes evident by looking the correlation plots for a few key nuclides: ^{88}Sr (Fig. 14), ^{138}Ba (Fig. 15), and ^{208}Pb (Fig. 16); we have selected these isotopes because they are the most abundant for the three

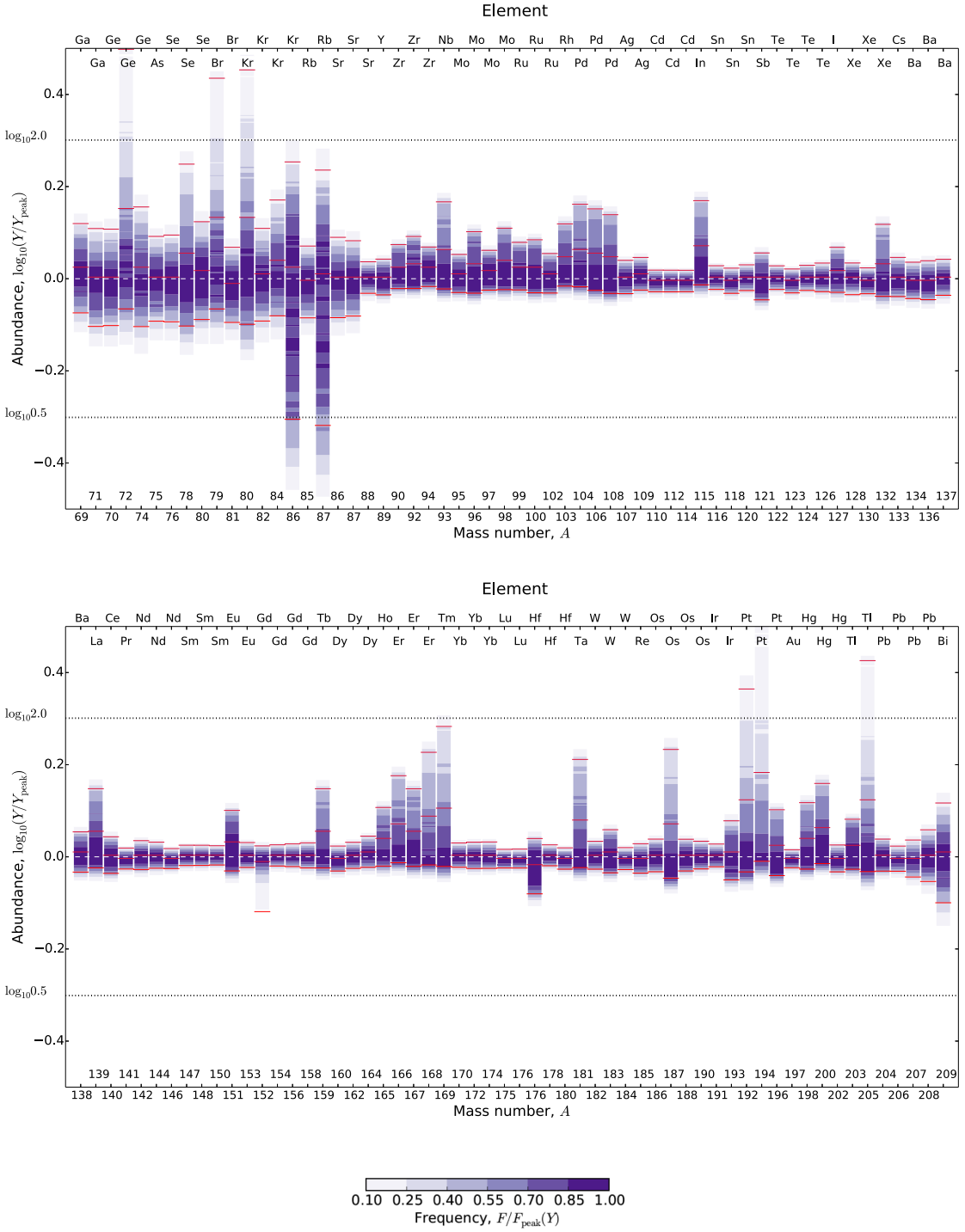

Figure 13. Total production uncertainties (same as Fig. 8) for the case with double the standard initial ^{13}C abundance ('2 × ^{13}C' case).

main peaks of the s-process path. In these plots, the correlation coefficients of the 900 reactions considered are shown, and the five reactions with the highest correlations are listed. These plots explain the main reason why these two or three neutron captures are not level 1 key rates: more than one of them contributes to the total uncertainty. Indeed, it is very rare to have a strong correlation with more than one rate since correlations with different rates weaken each other. Examination of the plots reveals that for all three test nuclides, the ^{56}Fe(n, γ) and ^{64}Ni(n, γ) reactions have high correlation factors, albeit they are below our threshold of 0.65. Only at the second level do they appear as key rates, but since these three reactions significantly contribute to the uncertainty of so many nuclides, it makes them priority targets for future measurements. For two of these neutron-capture reactions, the reason for their importance is clear. ^{56}Fe(n, γ) affects the neutron/seed ratio, while ^{138}Ba(n, γ) is an important bottleneck in the reaction chain. We elucidate the role of ^{64}Ni(n, γ) by presenting Fig. 17, which shows the Maxwellian averaged cross-sections (MACS) at 30 keV for a range of Ni isotopes.

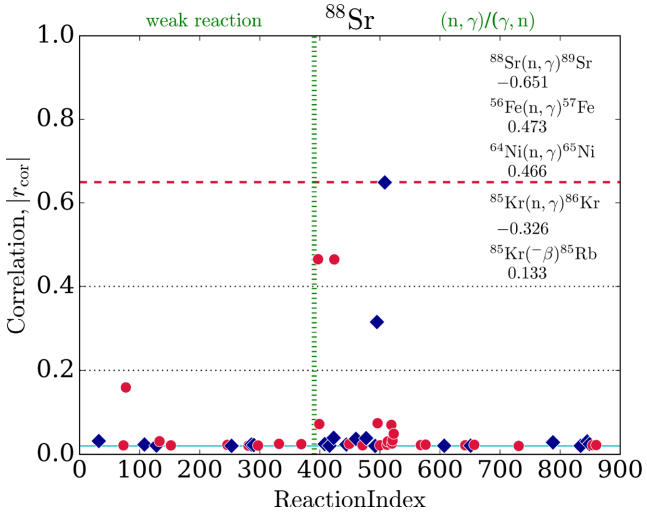

Figure 14. The correlation coefficients of reactions with respect to an abundance change of ^{88}Sr during the ^{13}C-pocket conditions. The absolute values of the coefficients are plotted against a reaction index number. Red circles stand for positive correlation and blue squares for negative correlation, respectively. Reaction indices in the range of 1–390 denote weak reactions and those in the range 391–900 identify neutron captures. The five reactions with the highest correlations are listed in the upper right corner. Note that, for better readability, reactions with correlation factors $|r_{cor}| < 0.02$ are omitted from this plot.

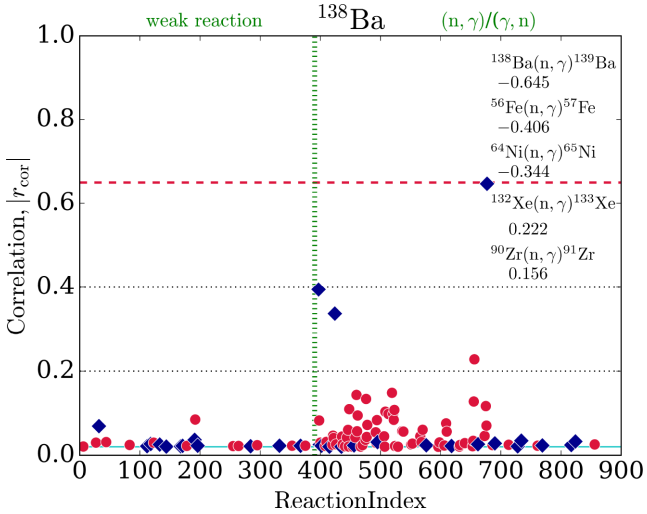

Figure 15. Same as for Fig. 14 for ^{138}Ba.

The even-neutron isotopes generally have smaller MACS values, reducing with increasing number of neutrons. The small value for ^{64}Ni means that ^{64}Ni becomes an effective bottleneck in the reaction chain towards ^{65}Cu and all heavier nuclei in the s-process path. One further reaction that we highlight as being of possible interest is that of ^{140}Ce(n, γ), which although identified only at level 3, is found to be a key rate at this level for multiple nuclei.

3.5 Comparison to the weak s-process key rates

In Table 5, we compare the correlation coefficient for the key reactions for the main s-process, which are also relevant for the weak s-process (see Nishimura et al. 2017). Not all of the latter are level 1 key rates for the weak s-process but it is interesting to know

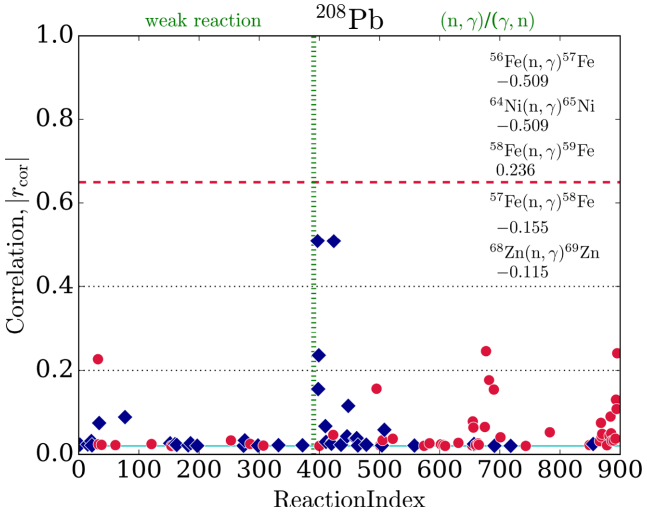

Figure 16. Same as for Fig. 14 for ^{208}Pb.

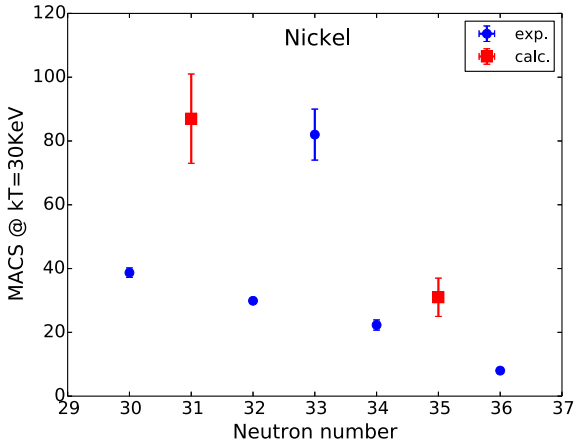

Figure 17. Maxwellian averaged cross-sections (MACS) at 30 keV for Ni isotopes (data taken by the website www.kadonis.org).

Table 5. Key rates dominating the production uncertainties for the ^{13}C-pocket conditions and also important for the weak s-process (column 1), nuclide for which the rate is highly correlated during the ^{13}C-pocket conditions (2), value of this correlation (3), isotopes for which the rate is correlated in the weak s-process production (4), and value of this correlation (5).

Key rates	Nuclide main s-	$r_{cor,0}$ main s-	Nuclide weak s-	$r_{cor,0}$ weak s-
^{72}Ge(n, γ)^{73}Ge	^{72}Ge	−0.93	^{72}Ge	−0.85
^{74}Ge(n, γ)^{75}Ge	^{74}Ge	−0.97	^{74}Ge	−0.44
^{75}As(n, γ)^{76}As	^{75}As	−0.86	^{75}As	−0.50
^{78}Se(n, γ)^{79}Se	^{78}Se	−0.96	^{78}Se	−0.71
^{84}Kr(n, γ)^{85}Kr	^{84}Kr	−0.99	^{84}Kr	−0.49
^{85}Kr(n, γ)^{86}Kr	^{86}Kr	0.88	^{86}Kr	0.84

which rate uncertainties affect predictions for both the main and weak s-process. In particular, ^{72}Ge(n, γ)^{73}Ge, ^{78}Se(n, γ)^{79}Se, and ^{85}Kr(n, γ)^{86}Kr are key rates with very high correlations for both the main and weak s-process. Therefore, a more precise measurement of these rates will enable more precise nucleosynthesis predictions for both processes.

3.6 Opportunities for improved nuclear data

A significant number of key reactions have been identified, which thus become the focus for future experimental work. Of these, the vast majority are of (n,γ) type, with the remainder being beta-decays. By the nature of the scenario being explored, all the reactions lie along or close to the valley of stability, and consequently the targets required for (n,γ) studies are stable or long lived such that solid or gaseous targets of sufficiently rich isotopic content may be acquired.

Table A1 lists the key reactions obtained in the present MC study. Before embarking on an experimental investigation of any of the listed reactions, two issues have to be considered, which are connected to the possible impact of a measurement. The first concerns the fact that a straightforward measurement of a cross-section in the laboratory yields the cross-section for the reaction proceeding on the ground state of the target nuclei. Depending on the plasma temperature T, however, a considerable fraction of nuclei in a star are in excited states and reactions on those have to be predicted by theory. The ground-state contribution to the stellar rate (Rauscher 2012a,b)

$$X_0(T) = \frac{2J_0+1}{G(T)}\frac{\mathcal{R}_{\rm g.s.}(T)}{\mathcal{R}^*(T)} \qquad (2)$$

quantifies the fraction of the stellar rate which can be constrained by such a cross-section measurement. Here, J_0 is the spin of the ground state and $G(T)$ is the nuclear partition function of the target nucleus. The reaction rate obtained by energy-averaging the ground-state cross-sections is denoted by $\mathcal{R}_{\rm g.s.}$ and the full stellar rate, including reactions on excited states, by $\mathcal{R}^*$. As described in Rauscher et al. (2016), the X_0 were also used to construct the temperature dependence of the rate uncertainties. An experiment will only be able to significantly reduce uncertainties for reactions with large ground-state contributions to the stellar rate. Although the stellar temperatures encountered in the s-process are comparatively low, it has been shown in Rauscher (2012b) and Rauscher et al. (2011) that non-negligible excited-state contributions appear for a number of nuclei also in the s-process, especially in the rare-earth region.

For convenience, the ground-state contributions X_0 at two s-process temperatures are given for each key neutron capture in Table A1. Most of the reactions have a ground-state contribution of unity, meaning a laboratory experiment may provide the relevant nuclear data.

The other issue to be considered before selecting a target for a measurement is that key rates in our definition are identified by the strength of the correlation factor, which identifies reactions that contribute most to the uncertainty of a particular nuclide's abundance relative to the contributions of all other reactions. It is important to remember that this does not indicate whether that abundance uncertainty itself is large or small, and hence whether it is of acute interest for improvement – for this, one must cross-reference with Table 3 or Fig. 8 to identify the nuclides having the largest uncertainties in their abundance. Doing so reveals where there is scope for updates to the reaction rate library to be useful. In several cases, there are already new data published or presently under analysis that are not yet included; these are detailed below. For others, new precision data are encouraged.

The Ge(n,γ) reactions have recently been subjected to measurements by the n_TOF collaboration (Lederer et al. 2014) and the data are presently being analysed. The ^{78}Se(n,γ) reaction is the subject of a near-future study (Lederer-Woods & Murphy 2017) that is motivated in part by previous work (Nishimura et al. 2017) from this paper's authorship. ^{79}Se(n,γ) is a well-known branching point for the main s-process and is the topic of another near-future n_TOF study (Domingo-Pardo 2014). There are also established intentions to pursue Kr(n,γ) experiments (Reifarth 2013). A n_TOF study of ^{93}Zr(n,γ) is already published (Tagliente et al. 2013), but it is noted that the conclusions drawn were limited by the relatively low enrichment (c. 20 per cent) of the target that was available.

Our MC process reveals a cluster of Rh and Pd nuclides with slightly increased abundance uncertainties around mass 105; the associated level 1 key reaction rates are also identified. New experimental time of flight data for neutron captures on Pd isotopes, covering the 15–100 keV region, has been provided by Terada et al. (2014). These report uncertainties improved now to the level of <6 per cent. The data for ^{106}Pd are interesting as they appear to show a significant (15–22 per cent) reduction compared to previous data. ^{115}In has a raised abundance uncertainty, identified here as due to the uncertainty in the ^{115}In(n,γ) reaction rate. New data are available here also (Katabuchi et al. 2015) that show agreement with another earlier data set but which disagree (at the level of ∼17 per cent) with other data sets and evaluations. Further clarification is required.

For the ^{132}Xe(n,γ) reaction, the accepted rate is based on the activation study of Beer (1991) that has an experimental uncertainty ∼8.5 per cent in the neutron capture cross-section at $kT = 30$ keV. In the case of the ^{159}Tb(n,γ) reaction, the reaction rate used here, and its uncertainty, is based on an average of the ENDFB71 and JENDL40 evaluated libraries, which in turn are based on several data sets that themselves show some disagreement (see e.g. Lepine, Douglas & Maia 1972; Mizumoto, Macklin & Halperin 1978). The ^{166}Er, ^{168}Er, and ^{169}Tm(n,γ) reactions see a similar situation. Precision neutron capture data are needed.

Laboratory measurements of neutron capture cross-sections are typically constrained to investigation of capture to ground states. Consequently, despite precision measurements, the possibility of capture on thermally excited states leads to overall greater uncertainties. Such is the case for the ^{169}Tm(n,γ), ^{181}Ta(n,γ), and ^{187}Os(n,γ) reactions that are identified as the level 1 key rates responsible for the increased uncertainties in the ^{169}Tm, ^{181}Ta, and ^{187}Os abundances. Despite relatively well-measured neutron capture cross-sections, excited states at 8.4, 6.2, and 9.8 keV, respectively, lead to the abundance variations seen in the current study that will be hard to improve upon by experiment.

Three other nuclides are determined to have poorly constrained abundances: $^{192,\,194}$Pt and ^{205}Pb. The reaction rate library used throughout this study provides only theoretical rates for the associated key reactions, for which our approach has been to consistently assign an uncertainty factor of 2. In fact, recent experimental data now exist for the $^{192,\,194}$Pt(n,γ) level 1 key rates (Koehler & Guber 2013) and thus the new abundance uncertainties for $^{192,\,194}$Pt are expected to best represented by Fig. 10. This provides a useful illustration of the improvement that new data can provide.

Several further reactions are of particular interest because of their broader impact: ^{56}Fe(n,γ), ^{64}Ni(n,γ), ^{138}Ba(n,γ), and ^{140}Ce(n,γ) are identified as level 2 and 3 reactions for a large number of nuclear abundances. For the first of these, there are a number of published data sets (Macklin, Pasma & Gibbons 1964; Allen et al. 1976, 1982; Wang et al. 2010), resulting in an uncertainty of around 10 per cent, but given the role of neutron capture on seed ^{56}Fe nuclei in this and other nucleosynthesis environments, greater precision is still needed. For the ^{64}Ni(n,γ) reaction, a recent measurement of the thermal neutron capture cross-section has been made (Shivashankar

et al. 2016) and an experiment is approved at the n_TOF facility (Tain et al. 2006). In the case of ^{138}Ba(n γ), Heil et al. (2005), using the ^{18}O(p, n) reaction that produces neutrons with a 5 keV thermal energy distribution, measured the Maxwellian-averaged neutron capture cross-section to a precision of about 4 per cent, in fair agreement with previous work (Beer, Corvi & Mutti 1997). The neutron capture on ^{140}Ce will be the subject of another near-future n_TOF measurement (Amaducci 2018). Its cross-section, in fact, albeit having been precisely measured at 25 keV (Käppeler et al. 1996), needs more precise data at lower energies, where the dominant resonance at 2.5 keV is poorly constrained.

Further experimental progress is anticipated thanks to new and planned facilities. At CERN, the second experimental area at n_TOF (Weiss et al. 2015) has a shorter flight path to deliver higher neutron fluxes, while the FRANZ (Alzubaidi et al. 2016) facility at the University of Frankfurt (Germany) and SARAF (Mardor & GuberBerkovits 2013) at the Soreq research centre (Israel) should soon deliver significantly higher fluxes, and thus sensitivity and precision.

4 CONCLUSIONS

For the first time we have performed a comprehensive, large-scale MC study for the main s-process in low-mass stars, varying reactions on targets from Fe to Bi. Temperature-dependent stellar reaction rate uncertainties were individually assigned to the reactions, allowing a quantification of the uncertainties in final abundances.

We found that β-decay rate uncertainties affect only a few nuclei near s-process branchings, whereas most of the uncertainty in the final abundances is caused by uncertainties in neutron-capture rates either directly producing or destroying the nuclide of interest. Combined total nuclear uncertainties due to reactions on heavy elements are in general small (less than 50 per cent). This means that nuclear uncertainties for the main s-process will be dominated by uncertainties in well-known reactions involving light elements, such as neutron source, e.g. ^{13}C(α,n) ^{16}O, and neutron poisons.

We studied the dependence of the uncertainties and key rates on the astrophysical conditions found in stars of different masses or metallicities (neutron-to-seed ratio) by varying the initial abundance of ^{13}C. We found that the key reaction list established is relevant for the full range of conditions studied. We compared our results and method to past sensitivity studies focusing on the main s-process, in particular the comprehensive study of Koloczek et al. (2016). Our approach clearly determines the key rates that dominate the total uncertainties in the nucleosynthesis predictions (rather than showing that a reaction has an impact on a certain number of nuclides). This is important to ensure that the (re-)measurement of a key rate will significantly reduce the uncertainties in the final abundances. While the strongest globally affecting reactions found by Ko16 are almost all identified as key rates for a few nuclides, they only dominate the total uncertainties for a few nuclides. The main exceptions are three key reactions which stand out because they significantly affect the uncertainties of a larger number of nuclides. These are ^{56}Fe(n,γ), ^{64}Ni(n,γ), and ^{138}Ba(n,γ). Improved data for these reactions will lead to a strong global reduction in prediction uncertainties.

We also compared our key reaction list to the one we determined for the weak s-process (Nishimura et al. 2017). In particular, ^{72}Ge(n, γ)^{73}Ge, ^{78}Se(n, γ)^{79}Se, and ^{85}Kr(n, γ)^{86}Kr are key rates with very high correlations for both the main and weak s-process. Therefore, a more precise measurement of these rates will enable more precise nucleosynthesis predictions for both processes.

Finally, we discussed the prospect of reducing uncertainties in the key reactions identified in this study with future experiments. Since the key rates are for nuclides along the valley of stability, many have already been measured, which explains the small total uncertainties. Nevertheless, new improved measurements are feasible and several are already underway.

ACKNOWLEDGEMENTS

We thank U. Frischknecht for his initial help in the development of the MC framework and C. Lederer-Woods for her input regards the status of several experimental works. This work was partially supported by the European Research Council (grants GA 321263-FISH and EU-FP7-ERC-2012-St Grant 306901), the EU COST Action CA16117 (ChETEC) and the UK Science and Technology Facilities Council (grants ST/M000958/1, ST/M001067/1). This work used the DIRAC Shared Memory Processing system at the University of Cambridge, operated by the COSMOS Project at the Department of Applied Mathematics and Theoretical Physics on behalf of the STFC DiRAC HPC Facility (www.dirac.ac.uk). This equipment was funded by BIS National E-infrastructure capital grant ST/J005673/1, STFC capital grant ST/H008586/1, and STFC DiRAC Operations grant ST/K00333X/1. DiRAC is part of the National E-Infrastructure. This work also used the computing facilities of the Center for Computational Astrophysics (CfCA) of the National Astronomical Observatory of Japan and of the Yukawa Institute for Theoretical Physics (YITP) of the Kyoto University. GC acknowledges financial support from the European Union Horizon 2020 research and innovation programme under the Marie Skłodowska-Curie grant agreement no. 664931. NN acknowledges financial support from MEXT Japan (Priority Issue on Post K Computer: Elucidation of the fundamental laws and evolution of the universe). The University of Edinburgh is a charitable body, registered in Scotland, with Registration No. SC005336.

REFERENCES

Abia C., Busso M., Gallino R., Domínguez I., Straniero O., Isern J., 2001, ApJ, 559, 1117
Abia C. et al., 2002, ApJ, 579, 817
Aikawa M., Arnould M., Goriely S., Jorissen A., Takahashi K., 2005, A&A, 441, 1195
Allen B., Musgrove A. L., Boldeman J., Kenny M., 1976, Nucl. Phys., A269, 408
Allen B., Musgrove A. L., Taylor R., Macklin R., 1982, Nucl. Sci. Eng., 82, 230
Alzubaidi S. et al., 2016, Eur. Phys. J. Plus, 131, 124
Amaducci S., 2018, CERN Proposal INTC-2018-002; INTC-P-533
Battino U. et al., 2016, ApJ, 827, 30
Beer H., 1991, ApJ, 375, 823
Beer H., Corvi F., Mutti P., 1997, ApJ, 474, 843
Burbidge E. M., Burbidge G. R., Fowler W. A., Hoyle F., 1957, Rev. Mod. Phys., 29, 547
Busso M., Gallino R., Lambert D. L., Travaglio C., Smith V. V., 2001, ApJ, 557, 802
Cameron A. G. W., 1957, PASP, 69, 201
Cescutti G., Valentini M., François P., Chiappini C., Depagne E., Christlieb N., Cortés C., 2016, A&A, 595, A91
Cristallo S., Straniero O., Gallino R., Piersanti L., Domínguez I., Lederer M. T., 2009, ApJ, 696, 797
Cristallo S., Straniero O., Lederer M. T., Aringer B., 2007, ApJ, 667, 489
Cristallo S., Straniero O., Piersanti L., Gobrecht D., 2015, ApJS, 219, 40
Cristallo S. et al., 2011, ApJS, 197, 17
Cristallo S. et al., 2018, ApJ, 859,105

Cyburt R. H. et al., 2010, ApJS, 189, 240
Dillmann I., Heil M., Käppeler F., Plag R., Rauscher T., Thielemann F.-K., 2006, in Woehr A., Aprahamian A., eds, AIP Conf. Ser. Vol. 819, Capture Gamma-Ray Spectroscopy and Related Topics. p. 123
Domingo-Pardo C., 2014, CERN Proposal INTC-2014-005; INTC-I-155
Freiburghaus C., Rauscher T., 1999, Reaction Rate Library in REACLIB Format, available at http://nucastro.org/reaclib
Frischknecht U. et al., 2016, MNRAS, 456, 1803
Gallino R., Arlandini C., Busso M., Lugaro M., Travaglio C., Straniero O., Chieffi A., Limongi M., 1998, ApJ, 497, 388
Goriely S., 1999, A&A, 342, 881
Heil M., Dababneh S., Juseviciute A., Kappeler F., Plag R., Reifarth R., O'Brien S., 2005, Phys. Rev. C, 71, 025803
Herwig F., 2005, ARA&A, 43, 435
Iben I., Jr, 1976, ApJ, 208, 165
Karakas A. I., Lugaro M., 2016, ApJ, 825, 26
Katabuchi T., Tsuda H., Terada K., Igashira M., 2015, Prog. Nucl. Energy, 82, 107
Koehler P., Guber K., 2013, Phys. Rev. C, 88, 035802
Koloczek A. et al., 2016, At. Data Nucl. Data Tables, 108, 1
Käppeler F., Gallino R., Bisterzo S., Aoki W., 2011, Rev. Mod. Phys., 83, 157
Käppeler F., Toukan K. A., Schumann M., Mengoni A., 1996, Phys. Rev. C, 53, 1397
Lederer-Woods C., Murphy A. St. J., 2017, CERN Proposal INTC-2017-038; INTC-P-509
Lederer C. et al., 2014, CERN Proposal INTC-2013-021; INTC-P-381
Lepine J., Douglas R., Maia H., 1972, Nucl. Phys. A, 83, 196
Macklin R., Pasma P., Gibbons J., 1964, Phys. Rev., 136, B695
Mardor I., GuberBerkovits D., 2013, Nucl. Phys. News, 25, 16
Mizumoto M., Macklin R., Halperin J., 1978, Phys. Rev. C, 17, 522
Nishimura N., Hirschi R., Rauscher T., Murphy A. St. J., Cescutti G., 2017, MNRAS, 469, 1752
Nishimura N., Rauscher T., Hirschi R., Murphy A. St. J., Cescutti G., Travaglio C., 2018, MNRAS, 474, 3133
Nishimura N. et al., 2014, in Jeong S., Imai N., Miyatake H., Kajino T., eds, AIP Conf. Ser. Vol. 1594, American Institute of Physics Conference Series. p. 146
Paxton B., Bildsten L., Dotter A., Herwig F., Lesaffre P., Timmes F., 2011, ApJS, 192, 3
Prantzos N., Abia C., Limongi M., Chieffi A., Cristallo S., 2018, MNRAS, 476, 3432
Rauscher T., 2012a, ApJS, 201, 26
Rauscher T., 2012b, ApJ, 755, L10
Rauscher T., Mohr P., Dillmann I., Plag R., 2011, ApJ, 738, 143
Rauscher T., Nishimura N., Cescutti G., Hirschi R., Murphy A. St. J., 2018, AIP Conf. Ser. Vol. 1947, American Institute of Physics Conference Series. p. 020015
Rauscher T., Nishimura N., Hirschi R., Cescutti G. A. St. J. M., Heger A., 2016, MNRAS, 463, 4153
Rauscher T., Thielemann F.-K., 2000, At. Data Nucl. Data Tables, 75, 1
Reifarth R., 2013, ERC Consolidator Grant PE2, ERC-2013-CoG 'NAUTILUS'
Schwarzschild M., Härm R., 1965, ApJ, 142, 855
Shivashankar B. et al., 2016, J. Radioanal. Nucl. Chem., 292, 745
Sneden C., Cowan J. J., Gallino R., 2008, ARA&A, 46, 241
Straniero O., Gallino R., Busso M., Chieffi A., Raiteri C. M., Limongi M., Salaris M., 1995, ApJ, 440, L85
Straniero O., Gallino R., Cristallo S., 2006, Nucl. Phys. A, 777, 311
Tagliente G. et al., 2013, Phys. Rev. C, 87, 014622
Tain J. et al., 2006, CERN Proposal INTC-2006-12; INTC-P-208
Takahashi K., Yokoi K., 1987, At. Data Nucl. Data Tables, 36, 375
Terada K., Matsuhashi T., Hales B., Katabuchi T., Igashira M., 2014, Nucl. Data Sheets, 119, 147
Trippella O., Busso M., Palmerini S., Maiorca E., Nucci M. C., 2016, ApJ, 818, 125
Wang T. et al., 2010, Nucl. Instrum. Methods Phys. Res. B, 268, 440
Weiss C. et al., 2015, Nucl. Instrum. Methods, 799, 90
Xu Y., Goriely S., Jorissen A., Chen G. L., Arnould M., 2013, A&A, 549, A106
Zamora O., Abia C., Plez B., Domínguez I., Cristallo S., 2009, A&A, 508, 909

APPENDIX: KEY RATES FOR DOUBLE AND HALF OF THE INITIAL ^{13}C ABUNDANCE

As explained in Section 3.3, the tables in this Appendix are provided to assess the sensitivity of the key rate list to the astrophysical conditions. We list in Table A1, the key rates for the 'standard' ^{13}C-pocket case and the corresponding total uncertainties are shown in Fig. 8. In Table A2, we list the key rates for the '0.5 $\times$ ^{13}C' case and the corresponding total uncertainties are shown in Fig. 12. Similarly, in Table A3, we list the key rates for the '2 $\times$ ^{13}C' case and the corresponding total uncertainties are shown in Fig. 13. The reference key reaction list is that of the 'standard' case given in Table A1. The other two tables are presented for discussion and reference only and should not be used to extract key rates. Finally, in Table A4, the key rates for the TP phase are presented and the corresponding total uncertainties are shown in Fig. 9.

Table A1. The key reaction rates for the standard model. Key rates in levels 1−3 are shown, along with their correlation factors r_{cor0}, r_{cor1}, and r_{cor2}, respectively. Not all s-process nuclides analysed are listed but only those for which key rates were found. Also shown for each rate are the ground state contributions X_0 to the stellar rate of the (n,γ) reaction and uncertainty factors of the β-decay rate at two plasma temperatures, respectively.

Nuclide	$r_{cor,0}$	$r_{cor,1}$	$r_{cor,2}$	Key rate Level 1	Key rate Level 2	Key rate Level 3	X_0 (8, 30 keV)	Weak rate uncertainty factor (8, 30 keV)
^{69}Ga	−0.77			^{69}Ga(n, γ)^{70}Ga			1.00, 1.00	
	−0.34	−0.67			^{64}Ni(n, γ)^{65}Ni		1.00, 1.00	
^{71}Ga	−0.89			^{71}Ga(n, γ)^{72}Ga			1.00, 1.00	
^{70}Ge	−0.87			^{70}Ge(n, γ)^{71}Ge			1.00, 1.00	
	−0.27	−0.66			^{64}Ni(n, γ)^{65}Ni		1.00, 1.00	
^{72}Ge	−0.93			^{72}Ge(n, γ)^{73}Ge			1.00, 1.00	
^{74}Ge	−0.97			^{74}Ge(n, γ)^{75}Ge			1.00, 1.00	
^{75}As	−0.86			^{75}As(n, γ)^{76}As			1.00, 1.00	
^{76}Se	−0.89			^{76}Se(n, γ)^{77}Se			1.00, 1.00	
^{78}Se	−0.97			^{78}Se(n, γ)^{79}Se			1.00, 1.00	
^{80}Se	−0.96			^{80}Se(n, γ)^{81}Se			1.00, 1.00	
^{79}Br	−0.94			^{79}Se(n, γ)^{80}Se			1.00, 1.00	
^{81}Br	−0.74			^{81}Br(n, γ)^{82}Br			1.00, 1.00	
^{80}Kr	−0.90			^{79}Se(n, γ)^{80}Se			1.00, 1.00	
	0.24	0.85			^{79}Se(β^-)^{79}Br			1.30, 1.49
^{82}Kr	−0.97			^{82}Kr(n, γ)^{83}Kr			1.00, 1.00	
^{84}Kr	−0.98			^{84}Kr(n, γ)^{85}Kr			1.00, 1.00	
^{86}Kr	0.88			^{85}Kr(n, γ)^{86}Kr			1.00, 1.00	
	−0.43	−0.95			^{85}Kr(β^-)^{85}Rb			1.30, 1.30
	−0.12	−0.28	−1.00			^{86}Kr(n, γ)^{87}Kr	1.00, 1.00	
^{85}Rb	−0.86			^{85}Rb(n, γ)^{86}Rb			1.00, 1.00	
^{87}Rb	0.86			^{85}Kr(n, γ)^{86}Kr			1.00, 1.00	
	−0.41	−0.85			^{85}Kr(β^-)^{85}Rb			1.30, 1.30
	0.20	0.39	0.77			^{86}Kr(n, γ)^{87}Kr	1.00, 1.00	
^{86}Sr	−0.94			^{86}Sr(n, γ)^{87}Sr			1.00, 1.00	
^{87}Sr	−0.92			^{87}Sr(n, γ)^{88}Sr			1.00, 1.00	
^{88}Sr	−0.65			^{88}Sr(n, γ)^{89}Sr			1.00, 1.00	
	0.47	0.69			^{56}Fe(n, γ)^{57}Fe		1.00, 1.00	
	0.47	0.68			^{64}Ni(n, γ)^{65}Ni		1.00, 1.00	
	0.06	0.11	0.65			^{58}Fe(n, γ)^{59}Fe	1.00, 1.00	
^{89}Y	−0.83			^{89}Y(n, γ)^{90}Y			1.00, 1.00	
	0.33	0.67			^{56}Fe(n, γ)^{57}Fe		1.00, 1.00	
	0.34	0.68			^{64}Ni(n, γ)^{65}Ni		1.00, 1.00	
	0.07	0.15	0.67			^{58}Fe(n, γ)^{59}Fe	1.00, 1.00	
^{90}Zr	−0.89			^{90}Zr(n, γ)^{91}Zr			1.00, 1.00	
	0.28	0.68			^{64}Ni(n, γ)^{65}Ni		1.00, 1.00	
^{92}Zr	−0.92			^{92}Zr(n, γ)^{93}Zr			1.00, 1.00	
	0.22	0.67			^{64}Ni(n, γ)^{65}Ni		1.00, 1.00	
^{94}Zr	−0.86			^{94}Zr(n, γ)^{95}Zr			1.00, 1.00	
	0.30	0.65			^{64}Ni(n, γ)^{65}Ni		1.00, 1.00	
^{93}Nb	−0.97			^{93}Zr(n, γ)^{94}Zr			1.00, 1.00	
	0.14	0.67			^{64}Ni(n, γ)^{65}Ni		1.00, 1.00	
^{95}Mo	−0.85			^{95}Mo(n, γ)^{96}Mo			1.00, 1.00	
	0.29	0.65			^{64}Ni(n, γ)^{65}Ni		1.00, 1.00	
^{96}Mo	−0.94			^{96}Mo(n, γ)^{97}Mo			1.00, 1.00	
^{97}Mo	−0.87			^{97}Mo(n, γ)^{98}Mo			1.00, 1.00	
^{98}Mo	−0.94			^{98}Mo(n, γ)^{99}Mo			1.00, 1.00	
^{99}Ru	−0.91			^{99}Tc(n, γ)^{100}Tc			1.00, 1.00	
^{100}Ru	−0.93			^{100}Ru(n, γ)^{101}Ru			1.00, 1.00	
^{102}Ru	−0.86			^{102}Ru(n, γ)^{103}Ru			1.00, 1.00	
^{103}Rh	−0.95			^{103}Rh(n, γ)^{104}Rh			0.95, 0.80	
^{104}Pd	−0.97			^{104}Pd(n, γ)^{105}Pd			1.00, 1.00	
^{106}Pd	−0.97			^{106}Pd(n, γ)^{107}Pd			1.00, 1.00	
^{108}Pd	−0.96			^{108}Pd(n, γ)^{109}Pd			1.00, 1.00	
^{107}Ag	−0.81			^{107}Pd(n, γ)^{108}Pd			1.00, 1.00	
^{109}Ag	−0.80			^{109}Ag(n, γ)^{110}Ag			1.00, 1.00	
^{110}Cd	−0.41	−0.48	−0.71			^{110}Cd(n, γ)^{111}Cd	1.00, 1.00	
^{112}Cd	−0.40	−0.45	−0.69			^{112}Cd(n, γ)^{113}Cd	1.00, 1.00	
^{114}Cd	−0.36	−0.43	−0.65			^{114}Cd(n, γ)^{115}Cd	1.00, 1.00	
^{115}In	−0.97			^{115}In(n, γ)^{116}In			1.00, 1.00	

Table A1 – *continued*

Nuclide	$r_{cor,0}$	$r_{cor,1}$	$r_{cor,2}$	Key rate Level 1	Key rate Level 2	Key rate Level 3	X_0 (8, 30 keV)	Weak rate uncertainty factor (8, 30 keV)
^{116}Sn	−0.51	−0.58	−0.78			^{116}Sn(n, γ)^{117}Sn	1.00, 1.00	
^{118}Sn	−0.59	−0.67			^{118}Sn(n, γ)^{119}Sn		1.00, 1.00	
^{120}Sn	−0.57	−0.67			^{120}Sn(n, γ)^{121}Sn		1.00, 1.00	
^{121}Sb	−0.92			^{121}Sb(n, γ)^{122}Sb			0.98, 0.93	
^{124}Te	−0.53	−0.65	−0.76			^{124}Te(n, γ)^{125}Te	1.00, 1.00	
^{126}Te	−0.69			^{126}Te(n, γ)^{127}Te			1.00, 1.00	
^{127}I	−0.92			^{127}I(n, γ)^{128}I			1.00, 0.99	
^{128}Xe	0.66			^{128}I(β^-)^{128}Xe				1.64, 5.42
^{130}Xe	−0.57	−0.71			^{130}Xe(n, γ)^{131}Xe		1.00, 1.00	
^{132}Xe	−0.97			^{132}Xe(n, γ)^{133}Xe			1.00, 1.00	
^{133}Cs	−0.89			^{133}Cs(n, γ)^{134}Cs			1.00, 1.00	
^{134}Ba	−0.85			^{134}Ba(n, γ)^{135}Ba			1.00, 1.00	
^{136}Ba	−0.88			^{136}Ba(n, γ)^{137}Ba			1.00, 1.00	
^{137}Ba	−0.84			^{137}Ba(n, γ)^{138}Ba			1.00, 1.00	
^{138}Ba	−0.65	−0.73			^{138}Ba(n, γ)^{139}Ba		1.00, 1.00	
^{139}La	−0.87			^{139}La(n, γ)^{140}La			1.00, 1.00	
	0.36	0.83			^{138}Ba(n, γ)^{139}Ba		1.00, 1.00	
^{140}Ce	0.59	0.65			^{138}Ba(n, γ)^{139}Ba		1.00, 1.00	
	−0.39	−0.42	−0.90			^{140}Ce(n, γ)^{141}Ce	1.00, 1.00	
^{141}Pr	0.59	0.65			^{138}Ba(n, γ)^{139}Ba		1.00, 1.00	
	0.31	0.33	0.85			^{140}Ce(n, γ)^{141}Ce	1.00, 1.00	
^{142}Nd	−0.31	−0.34	−0.67			^{142}Nd(n, γ)^{143}Nd	1.00, 1.00	
^{146}Nd	0.28	0.30	0.76			^{140}Ce(n, γ)^{141}Ce	1.00, 1.00	
^{147}Sm	0.28	0.30	0.74			^{140}Ce(n, γ)^{141}Ce	1.00, 1.00	
^{148}Sm	0.28	0.29	0.74			^{140}Ce(n, γ)^{141}Ce	1.00, 1.00	
^{150}Sm	0.28	0.29	0.76			^{140}Ce(n, γ)^{141}Ce	1.00, 1.00	
^{151}Eu	−0.70			^{151}Eu(n, γ)^{152}Eu			0.89, 0.79	
	0.19	0.29	0.68			^{140}Ce(n, γ)^{141}Ce	1.00, 1.00	
^{152}Gd	0.59	0.61	0.79			^{151}Sm(β^-)^{151}Eu		3.60, 5.42
^{154}Gd	0.27	0.29	0.71			^{140}Ce(n, γ)^{141}Ce	1.00, 1.00	
^{156}Gd	0.27	0.28	0.67			^{140}Ce(n, γ)^{141}Ce	1.00, 1.00	
^{159}Tb	−0.79			^{159}Tb(n, γ)^{160}Tb			1.00, 0.98	
	0.16	0.29	0.74			^{140}Ce(n, γ)^{141}Ce	1.00, 1.00	
^{164}Dy	−0.35	−0.38	−0.71			^{164}Dy(n, γ)^{165}Dy	1.00, 0.97	
^{165}Ho	−0.68			^{165}Ho(n, γ)^{166}Ho			1.00, 1.00	
	0.19	0.28	0.72			^{140}Ce(n, γ)^{141}Ce	1.00, 1.00	
^{166}Er	−0.81			^{166}Er(n, γ)^{167}Er			1.00, 0.98	
	0.15	0.28	0.72			^{140}Ce(n, γ)^{141}Ce	1.00, 1.00	
^{167}Er	−0.78			^{167}Er(n, γ)^{168}Er			1.00, 1.00	
	0.17	0.28	0.72			^{140}Ce(n, γ)^{141}Ce	1.00, 1.00	
^{168}Er	−0.86			^{168}Er(n, γ)^{169}Er			1.00, 0.98	
	0.11	0.28	0.72			^{140}Ce(n, γ)^{141}Ce	1.00, 1.00	
^{169}Tm	−0.90			^{169}Tm(n, γ)^{170}Tm			0.51, 0.42	
	0.10	0.28	0.71			^{140}Ce(n, γ)^{141}Ce	1.00, 1.00	
^{175}Lu	0.26	0.27	0.69			^{140}Ce(n, γ)^{141}Ce	1.00, 1.00	
^{176}Lu	0.25	0.26	0.65			^{140}Ce(n, γ)^{141}Ce	1.00, 1.00	
^{176}Hf	0.61	0.63	0.89			^{176}Lu(β^-)^{176}Hf		1.30, 1.33
^{181}Ta	−0.84			^{181}Ta(n, γ)^{182}Ta			0.61, 0.55	
	0.12	0.26	0.67			^{140}Ce(n, γ)^{141}Ce	1.00, 1.00	
^{183}W	−0.49	−0.51	−0.82			^{183}W(n, γ)^{184}W	0.99, 0.93	
^{187}Os	−0.86			^{187}Os(n, γ)^{188}Os			0.57, 0.46	
^{188}Os	−0.34	−0.35	−0.67			^{188}Os(n, γ)^{189}Os	1.00, 1.00	
^{193}Ir	−0.58	−0.59	−0.84			^{193}Ir(n, γ)^{194}Ir	1.00, 0.99	
^{192}Pt	−0.89			^{192}Pt(n, γ)^{193}Pt			1.00, 1.00	
^{194}Pt	−0.90			^{194}Pt(n, γ)^{195}Pt			1.00, 1.00	
^{196}Pt	−0.63	−0.65	−0.89			^{196}Pt(n, γ)^{197}Pt	1.00, 1.00	
^{198}Hg	−0.63	−0.65			^{198}Hg(n, γ)^{199}Hg		1.00, 1.00	
^{200}Hg	−0.67			^{200}Hg(n, γ)^{201}Hg			1.00, 1.00	
^{203}Tl	−0.48	−0.49	−0.78			^{203}Tl(n, γ)^{204}Tl	1.00, 1.00	
^{205}Tl	−0.87			^{205}Pb(n, γ)^{206}Pb			0.83, 0.82	
^{209}Bi	0.53	0.56	0.71			^{208}Pb(n, γ)^{209}Pb	1.00, 1.00	

Table A2. Key reaction rates for the model with half the initial ^{13}C abundance ('0.5 × ^{13}C' case). Key rates in levels 1−3 are shown, along with their correlation factors r_{cor0}, r_{cor1}, and r_{cor2}, respectively. Not all s-process nuclides analysed are listed but only those for which key rates were found. Also shown for each rate are the ground-state contributions of the (n,γ) reaction to the stellar rate and uncertainty factors of the β-decay rate at two plasma temperatures, respectively.

Nuclide	$r_{cor,0}$	$r_{cor,1}$	$r_{cor,2}$	Key rate Level 1	Key rate Level 2	Key rate Level 3	X_0 (8, 30 keV)	β-decay
^{69}Ga	−0.88			^{69}Ga(n, γ)^{70}Ga			1.00, 1.00	
	0.33	0.73			^{56}Fe(n, γ)^{57}Fe		1.00, 1.00	
	0.29	0.65			^{64}Ni(n, γ)^{65}Ni		1.00, 1.00	
^{71}Ga	−0.93			^{71}Ga(n, γ)^{72}Ga			1.00, 1.00	
	0.26	0.72			^{56}Fe(n, γ)^{57}Fe		1.00, 1.00	
	0.25	0.67			^{64}Ni(n, γ)^{65}Ni		1.00, 1.00	
	0.04	0.12	0.72			^{58}Fe(n, γ)^{59}Fe	1.00, 1.00	
^{70}Ge	−0.92			^{70}Ge(n, γ)^{71}Ge			1.00, 1.00	
	0.25	0.73			^{56}Fe(n, γ)^{57}Fe		1.00, 1.00	
	0.25	0.66			^{64}Ni(n, γ)^{65}Ni		1.00, 1.00	
	0.05	0.11	0.67			^{58}Fe(n, γ)^{59}Fe	1.00, 1.00	
^{72}Ge	−0.93			^{72}Ge(n, γ)^{73}Ge			1.00, 1.00	
	0.06	0.71			^{56}Fe(n, γ)^{57}Fe		1.00, 1.00	
	0.06	0.67			^{64}Ni(n, γ)^{65}Ni		1.00, 1.00	
	0.02	0.14	0.76			^{58}Fe(n, γ)^{59}Fe	1.00, 1.00	
^{74}Ge	−0.96	−0.96			^{74}Ge(n, γ)^{75}Ge		1.00, 1.00	
	0.05	0.06	0.73			^{58}Fe(n, γ)^{59}Fe	1.00, 1.00	
^{75}As	−0.83			^{75}As(n, γ)^{76}As			1.00, 1.00	
	0.37	0.69			^{56}Fe(n, γ)^{57}Fe		1.00, 1.00	
	0.36	0.68			^{64}Ni(n, γ)^{65}Ni		1.00, 1.00	
	0.10	0.18	0.73			^{58}Fe(n, γ)^{59}Fe	1.00, 1.00	
^{76}Se	−0.86			^{76}Se(n, γ)^{77}Se			1.00, 1.00	
	0.35	0.69			^{56}Fe(n, γ)^{57}Fe		1.00, 1.00	
	0.34	0.68			^{64}Ni(n, γ)^{65}Ni		1.00, 1.00	
	0.11	0.19	0.71			^{58}Fe(n, γ)^{59}Fe	1.00, 1.00	
^{78}Se	−0.97			^{78}Se(n, γ)^{79}Se			1.00, 1.00	
	0.12	0.67			^{56}Fe(n, γ)^{57}Fe		1.00, 1.00	
	0.12	0.68			^{64}Ni(n, γ)^{65}Ni		1.00, 1.00	
	0.05	0.21	0.67			^{58}Fe(n, γ)^{59}Fe	1.00, 1.00	
^{80}Se	−0.91			^{80}Se(n, γ)^{81}Se			1.00, 1.00	
	0.25	0.66			^{64}Ni(n, γ)^{65}Ni		1.00, 1.00	
^{79}Br	−0.94			^{79}Se(n, γ)^{80}Se			1.00, 1.00	
	0.05	0.65			^{64}Ni(n, γ)^{65}Ni		1.00, 1.00	
^{81}Br	−0.58	−0.59	−0.83			^{81}Br(n, γ)^{82}Br	1.00, 1.00	
^{80}Kr	−0.90			^{79}Se(n, γ)^{80}Se			1.00, 1.00	
	0.25	0.80			^{79}Se(β^-)^{79}Br			1.30, 1.49
^{82}Kr	−0.91			^{82}Kr(n, γ)^{83}Kr			1.00, 1.00	
	0.25	0.66			^{64}Ni(n, γ)^{65}Ni		1.00, 1.00	
^{84}Kr	−0.96			^{84}Kr(n, γ)^{85}Kr			1.00, 1.00	
	0.17	0.65			^{64}Ni(n, γ)^{65}Ni		1.00, 1.00	
^{86}Kr	0.88			^{85}Kr(n, γ)^{86}Kr			1.00, 1.00	
	−0.43	−0.97			^{85}Kr(β^-)^{85}Rb			1.30, 1.30
	−0.07	−0.12	−0.93			^{86}Kr(n, γ)^{87}Kr	1.00, 1.00	
^{85}Rb	−0.66			^{85}Rb(n, γ)^{86}Rb			1.00, 1.00	
	0.47	0.65			^{64}Ni(n, γ)^{65}Ni		1.00, 1.00	
^{87}Rb	0.84			^{85}Kr(n, γ)^{86}Kr			1.00, 1.00	
	−0.42	−0.82			^{85}Kr(β^-)^{85}Rb			1.30, 1.30
	0.24	0.48	0.88			^{86}Kr(n, γ)^{87}Kr	1.00, 1.00	
^{86}Sr	−0.85			^{86}Sr(n, γ)^{87}Sr			1.00, 1.00	
^{87}Sr	−0.81			^{87}Sr(n, γ)^{88}Sr			1.00, 1.00	
^{89}Y	−0.69			^{89}Y(n, γ)^{90}Y			1.00, 1.00	
^{90}Zr	−0.73			^{90}Zr(n, γ)^{91}Zr			1.00, 1.00	
^{92}Zr	−0.79			^{92}Zr(n, γ)^{93}Zr			1.00, 1.00	
^{94}Zr	−0.57	−0.71			^{94}Zr(n, γ)^{95}Zr		1.00, 1.00	
^{93}Nb	−0.92			^{93}Zr(n, γ)^{94}Zr			1.00, 1.00	
^{95}Mo	−0.64	−0.76			^{95}Mo(n, γ)^{96}Mo		1.00, 1.00	
^{96}Mo	−0.81			^{96}Mo(n, γ)^{97}Mo			1.00, 1.00	
	−0.25	−0.65			^{56}Fe(n, γ)^{57}Fe		1.00, 1.00	
^{97}Mo	−0.65			^{97}Mo(n, γ)^{98}Mo			1.00, 1.00	
	−0.34	−0.65			^{56}Fe(n, γ)^{57}Fe		1.00, 1.00	

Table A2 – *continued*

Nuclide	$r_{cor,0}$	$r_{cor,1}$	$r_{cor,2}$	Key rate Level 1	Key rate Level 2	Key rate Level 3	X_0 (8, 30 keV)	β-decay
^{98}Mo	−0.79			^{98}Mo(n, γ)^{99}Mo			1.00, 1.00	
	−0.29	−0.67			^{56}Fe(n, γ)^{57}Fe		1.00, 1.00	
^{99}Ru	−0.71			^{99}Tc(n, γ)^{100}Tc			1.00, 1.00	
	−0.33	−0.67			^{56}Fe(n, γ)^{57}Fe		1.00, 1.00	
^{100}Ru	−0.73			^{100}Ru(n, γ)^{101}Ru			1.00, 1.00	
	−0.32	−0.68			^{56}Fe(n, γ)^{57}Fe		1.00, 1.00	
^{102}Ru	−0.57	−0.68			^{102}Ru(n, γ)^{103}Ru		1.00, 1.00	
^{103}Rh	−0.79			^{103}Rh(n, γ)^{104}Rh			0.95, 0.80	
	−0.29	−0.69			^{56}Fe(n, γ)^{57}Fe		1.00, 1.00	
^{104}Pd	−0.86			^{104}Pd(n, γ)^{105}Pd			1.00, 1.00	
	−0.26	−0.69			^{56}Fe(n, γ)^{57}Fe		1.00, 1.00	
^{106}Pd	−0.85			^{106}Pd(n, γ)^{107}Pd			1.00, 1.00	
	−0.26	−0.70			^{56}Fe(n, γ)^{57}Fe		1.00, 1.00	
^{108}Pd	−0.83			^{108}Pd(n, γ)^{109}Pd			1.00, 1.00	
	−0.30	−0.70			^{56}Fe(n, γ)^{57}Fe		1.00, 1.00	
^{107}Ag	−0.48	−0.58	−0.84			^{107}Pd(n, γ)^{108}Pd	1.00, 1.00	
^{109}Ag	−0.46	−0.56	−0.82			^{109}Ag(n, γ)^{110}Ag	1.00, 1.00	
^{110}Cd	−0.52	−0.69			^{56}Fe(n, γ)^{57}Fe		1.00, 1.00	
^{112}Cd	−0.53	−0.70			^{56}Fe(n, γ)^{57}Fe		1.00, 1.00	
^{114}Cd	−0.54	−0.71			^{56}Fe(n, γ)^{57}Fe		1.00, 1.00	
^{115}In	−0.83			^{115}In(n, γ)^{116}In			1.00, 1.00	
	−0.30	−0.71			^{56}Fe(n, γ)^{57}Fe		1.00, 1.00	
^{116}Sn	−0.55	−0.70			^{56}Fe(n, γ)^{57}Fe		1.00, 1.00	
^{118}Sn	−0.57	−0.70			^{56}Fe(n, γ)^{57}Fe		1.00, 1.00	
^{120}Sn	−0.59	−0.71			^{56}Fe(n, γ)^{57}Fe		1.00, 1.00	
^{121}Sb	−0.50	−0.55	−0.83			^{121}Sb(n, γ)^{122}Sb	0.98, 0.93	
^{122}Te	−0.60	−0.71			^{56}Fe(n, γ)^{57}Fe		1.00, 1.00	
^{123}Te	−0.59	−0.71			^{56}Fe(n, γ)^{57}Fe		1.00, 1.00	
^{124}Te	−0.60	−0.71			^{56}Fe(n, γ)^{57}Fe		1.00, 1.00	
^{126}Te	−0.60	−0.70			^{56}Fe(n, γ)^{57}Fe		1.00, 1.00	
^{127}I	−0.44	−0.47	−0.77			^{127}I(n, γ)^{128}I	1.00, 0.99	
^{128}Xe	−0.59	−0.68			^{56}Fe(n, γ)^{57}Fe		1.00, 1.00	
^{130}Xe	−0.61	−0.70			^{56}Fe(n, γ)^{57}Fe		1.00, 1.00	
^{132}Xe	−0.53	−0.55	−0.81			^{132}Xe(n, γ)^{133}Xe	1.00, 1.00	
^{133}Cs	−0.58	−0.65			^{56}Fe(n, γ)^{57}Fe		1.00, 1.00	
^{134}Ba	−0.60	−0.66			^{56}Fe(n, γ)^{57}Fe		1.00, 1.00	
^{136}Ba	−0.60	−0.66			^{56}Fe(n, γ)^{57}Fe		1.00, 1.00	
^{137}Ba	−0.60	−0.66			^{56}Fe(n, γ)^{57}Fe		1.00, 1.00	
^{138}Ba	−0.62	−0.66			^{56}Fe(n, γ)^{57}Fe		1.00, 1.00	
^{159}Tb	−0.54	−0.58	−0.72			^{159}Tb(n, γ)^{160}Tb	1.00, 0.98	
^{166}Er	−0.59	−0.63	−0.76			^{166}Er(n, γ)^{167}Er	1.00, 0.98	
^{167}Er	−0.55	−0.59	−0.73			^{167}Er(n, γ)^{168}Er	1.00, 1.00	
^{168}Er	−0.68			^{168}Er(n, γ)^{169}Er			1.00, 0.98	
^{169}Tm	−0.77			^{169}Tm(n, γ)^{170}Tm			0.51, 0.42	
^{181}Ta	−0.74			^{181}Ta(n, γ)^{182}Ta			0.61, 0.55	
^{187}Os	−0.81			^{187}Os(n, γ)^{188}Os			0.57, 0.46	
^{193}Ir	−0.55	−0.59	−0.70			^{193}Ir(n, γ)^{194}Ir	1.00, 0.99	
^{192}Pt	−0.88			^{192}Pt(n, γ)^{193}Pt			1.00, 1.00	
^{194}Pt	−0.89			^{194}Pt(n, γ)^{195}Pt			1.00, 1.00	
^{196}Pt	−0.65			^{196}Pt(n, γ)^{197}Pt			1.00, 1.00	
^{198}Hg	−0.66			^{198}Hg(n, γ)^{199}Hg			1.00, 1.00	
^{200}Hg	−0.76			^{200}Hg(n, γ)^{201}Hg			1.00, 1.00	
^{203}Tl	−0.66			^{203}Tl(n, γ)^{204}Tl			1.00, 1.00	
^{205}Tl	−0.92			^{205}Pb(n, γ)^{206}Pb			0.83, 0.82	
^{207}Pb	−0.61	−0.62	−0.67			^{207}Pb(n, γ)^{208}Pb	1.00, 1.00	
^{209}Bi	−0.77			^{209}Bi(n, γ)^{210}Bi			1.00, 1.00	
	0.58	0.92			^{208}Pb(n, γ)^{209}Pb		1.00, 1.00	

Table A3. Key reaction rates for the model with double the initial ^{13}C abundance ('2 × ^{13}C' case). Key rates in levels 1−3 are shown, along with their correlation factors r_{cor0}, r_{cor1}, and r_{cor2}, respectively. Not all s-process nuclides analysed are listed but only those for which key rates were found. Also shown for each rate are the ground-state contributions of the (n,γ) reaction to the stellar rate and uncertainty factors of the β-decay rate at two plasma temperatures, respectively.

Nuclide	$r_{cor,0}$	$r_{cor,1}$	$r_{cor,2}$	Key rate Level 1	Key rate Level 2	Key rate Level 3	X_0 (8, 30 keV)	β-decay
^{69}Ga	−0.42	−0.43	−0.92			^{69}Ga(n, γ)^{70}Ga	1.00, 1.00	
^{71}Ga	−0.57	−0.58	−0.96			^{71}Ga(n, γ)^{72}Ga	1.00, 1.00	
^{70}Ge	−0.53	−0.55	−0.95			^{70}Ge(n, γ)^{71}Ge	1.00, 1.00	
^{72}Ge	−0.89			^{72}Ge(n, γ)^{73}Ge			1.00, 1.00	
	−0.19	−0.69			^{56}Fe(n, γ)^{57}Fe		1.00, 1.00	
	−0.17	−0.68			^{64}Ni(n, γ)^{65}Ni		1.00, 1.00	
^{74}Ge	−0.76			^{74}Ge(n, γ)^{75}Ge			1.00, 1.00	
	−0.40	−0.68			^{56}Fe(n, γ)^{57}Fe		1.00, 1.00	
	−0.41	−0.68			^{64}Ni(n, γ)^{65}Ni		1.00, 1.00	
^{75}As	−0.41	−0.46	−0.91			^{75}As(n, γ)^{76}As	1.00, 1.00	
^{76}Se	−0.46	−0.49	−0.93			^{76}Se(n, γ)^{77}Se	1.00, 1.00	
^{78}Se	−0.87			^{78}Se(n, γ)^{79}Se			1.00, 1.00	
	−0.27	−0.67			^{56}Fe(n, γ)^{57}Fe		1.00, 1.00	
	−0.29	−0.69			^{64}Ni(n, γ)^{65}Ni		1.00, 1.00	
^{80}Se	−0.67			^{80}Se(n, γ)^{81}Se			1.00, 1.00	
	−0.46	−0.67			^{56}Fe(n, γ)^{57}Fe		1.00, 1.00	
	−0.47	−0.69			^{64}Ni(n, γ)^{65}Ni		1.00, 1.00	
^{79}Br	−0.90			^{79}Se(n, γ)^{80}Se			1.00, 1.00	
	−0.19	−0.67			^{56}Fe(n, γ)^{57}Fe		1.00, 1.00	
	−0.19	−0.68			^{64}Ni(n, γ)^{65}Ni		1.00, 1.00	
^{81}Br	−0.61	−0.66			^{64}Ni(n, γ)^{65}Ni		1.00, 1.00	
	−0.26	−0.28	−0.75			^{81}Br(n, γ)^{82}Br	1.00, 1.00	
^{80}Kr	−0.86			^{79}Se(n, γ)^{80}Se			1.00, 1.00	
	0.24	0.64	0.84			^{79}Se(β^-)^{79}Br		1.30, 1.49
^{82}Kr	−0.64	−0.68			^{82}Kr(n, γ)^{83}Kr		1.00, 1.00	
^{84}Kr	−0.80			^{84}Kr(n, γ)^{85}Kr			1.00, 1.00	
	−0.36	−0.66			^{56}Fe(n, γ)^{57}Fe		1.00, 1.00	
	−0.37	−0.69			^{64}Ni(n, γ)^{65}Ni		1.00, 1.00	
^{86}Kr	0.85			^{85}Kr(n, γ)^{86}Kr			1.00, 1.00	
	−0.41	−0.84			^{85}Kr(β^-)^{85}Rb			1.30, 1.30
	−0.27	−0.52	−1.00			^{86}Kr(n, γ)^{87}Kr	1.00, 1.00	
^{85}Rb	−0.60	−0.65			^{64}Ni(n, γ)^{65}Ni		1.00, 1.00	
	−0.32	−0.36	−0.82			^{85}Rb(n, γ)^{86}Rb	1.00, 1.00	
^{87}Rb	0.87			^{85}Kr(n, γ)^{86}Kr			1.00, 1.00	
	−0.41	−0.89			^{85}Kr(β^-)^{85}Rb			1.30, 1.30
	−0.18	−0.39	−0.92			^{87}Rb(n, γ)^{88}Rb	1.00, 1.00	
^{86}Sr	−0.54	−0.58	−0.94			^{86}Sr(n, γ)^{87}Sr	1.00, 1.00	
^{87}Sr	−0.46	−0.53	−0.91			^{87}Sr(n, γ)^{88}Sr	1.00, 1.00	
^{88}Sr	−0.66			^{88}Sr(n, γ)^{89}Sr			1.00, 1.00	
	−0.41	−0.66			^{64}Ni(n, γ)^{65}Ni		1.00, 1.00	
^{89}Y	−0.81			^{89}Y(n, γ)^{90}Y			1.00, 1.00	
^{90}Zr	−0.92			^{90}Zr(n, γ)^{91}Zr			1.00, 1.00	
^{92}Zr	−0.94			^{92}Zr(n, γ)^{93}Zr			1.00, 1.00	
^{94}Zr	−0.89			^{94}Zr(n, γ)^{95}Zr			1.00, 1.00	
^{93}Nb	−0.97			^{93}Zr(n, γ)^{94}Zr			1.00, 1.00	
^{95}Mo	−0.88			^{95}Mo(n, γ)^{96}Mo			1.00, 1.00	
^{96}Mo	−0.96			^{96}Mo(n, γ)^{97}Mo			1.00, 1.00	
^{97}Mo	−0.89			^{97}Mo(n, γ)^{98}Mo			1.00, 1.00	
^{98}Mo	−0.95			^{98}Mo(n, γ)^{99}Mo			1.00, 1.00	
^{99}Ru	−0.92			^{99}Tc(n, γ)^{100}Tc			1.00, 1.00	
^{100}Ru	−0.94			^{100}Ru(n, γ)^{101}Ru			1.00, 1.00	
	0.10	0.48	0.65			^{86}Kr(n, γ)^{87}Kr	1.00, 1.00	
^{102}Ru	−0.88			^{102}Ru(n, γ)^{103}Ru			1.00, 1.00	
	0.15	0.47	0.65			^{86}Kr(n, γ)^{87}Kr	1.00, 1.00	
^{103}Rh	−0.95			^{103}Rh(n, γ)^{104}Rh			0.95, 0.80	
	0.09	0.47	0.66			^{86}Kr(n, γ)^{87}Kr	1.00, 1.00	
^{104}Pd	−0.97			^{104}Pd(n, γ)^{105}Pd			1.00, 1.00	
	0.07	0.47	0.66			^{86}Kr(n, γ)^{87}Kr	1.00, 1.00	

Table A3 – *continued*

Nuclide	$r_{cor,0}$	$r_{cor,1}$	$r_{cor,2}$	Key rate Level 1	Key rate Level 2	Key rate Level 3	X_0 (8, 30 keV)	β-decay
^{106}Pd	−0.97			^{106}Pd(n, γ)^{107}Pd			1.00, 1.00	
	0.07	0.65			^{85}Kr(β^-)^{85}Rb			1.30, 1.30
	0.05	0.46	0.67			^{86}Kr(n, γ)^{87}Kr	1.00, 1.00	
^{108}Pd	−0.97			^{108}Pd(n, γ)^{109}Pd			1.00, 1.00	
	0.10	0.65			^{85}Kr(β^-)^{85}Rb			1.30, 1.30
	0.05	0.45	0.67			^{86}Kr(n, γ)^{87}Kr	1.00, 1.00	
^{107}Ag	−0.82			^{107}Pd(n, γ)^{108}Pd			1.00, 1.00	
	0.19	0.65			^{85}Kr(β^-)^{85}Rb			1.30, 1.30
	0.14	0.46	0.67			^{86}Kr(n, γ)^{87}Kr	1.00, 1.00	
^{109}Ag	−0.81			^{109}Ag(n, γ)^{110}Ag			1.00, 1.00	
	0.19	0.65			^{85}Kr(β^-)^{85}Rb			1.30, 1.30
	0.17	0.45	0.67			^{86}Kr(n, γ)^{87}Kr	1.00, 1.00	
^{110}Cd	−0.67			^{85}Kr(n, γ)^{86}Kr			1.00, 1.00	
	−0.42	−0.71			^{110}Cd(n, γ)^{111}Cd		1.00, 1.00	
	0.23	0.31	0.67			^{86}Kr(n, γ)^{87}Kr	1.00, 1.00	
^{112}Cd	−0.69			^{85}Kr(n, γ)^{86}Kr			1.00, 1.00	
	−0.41	−0.68			^{112}Cd(n, γ)^{113}Cd		1.00, 1.00	
	0.23	0.33	0.69			^{86}Kr(n, γ)^{87}Kr	1.00, 1.00	
^{114}Cd	−0.70			^{85}Kr(n, γ)^{86}Kr			1.00, 1.00	
	−0.36	−0.63	−0.81			^{114}Cd(n, γ)^{115}Cd	1.00, 1.00	
^{115}In	−0.97			^{115}In(n, γ)^{116}In			1.00, 1.00	
	0.07	0.65			^{85}Kr(β^-)^{85}Rb			1.30, 1.30
	0.06	0.42	0.70			^{86}Kr(n, γ)^{87}Kr	1.00, 1.00	
^{116}Sn	−0.66			^{85}Kr(n, γ)^{86}Kr			1.00, 1.00	
	−0.50	−0.77			^{116}Sn(n, γ)^{117}Sn		1.00, 1.00	
	0.19	0.25	0.71			^{86}Kr(n, γ)^{87}Kr	1.00, 1.00	
^{118}Sn	−0.55	−0.81			^{118}Sn(n, γ)^{119}Sn		1.00, 1.00	
	0.18	0.19	0.74			^{86}Kr(n, γ)^{87}Kr	1.00, 1.00	
^{120}Sn	−0.65			^{85}Kr(n, γ)^{86}Kr			1.00, 1.00	
	−0.52	−0.76			^{120}Sn(n, γ)^{121}Sn		1.00, 1.00	
	0.17	0.22	0.79			^{86}Kr(n, γ)^{87}Kr	1.00, 1.00	
^{121}Sb	−0.89			^{121}Sb(n, γ)^{122}Sb			0.98, 0.93	
	0.09	0.32	0.79			^{86}Kr(n, γ)^{87}Kr	1.00, 1.00	
^{122}Te	−0.71			^{85}Kr(n, γ)^{86}Kr			1.00, 1.00	
	−0.34	−0.54	−0.80			^{122}Te(n, γ)^{123}Te	1.00, 1.00	
^{123}Te	−0.71			^{85}Kr(n, γ)^{86}Kr			1.00, 1.00	
	0.35	0.54	0.80			^{123}Te(n, γ)^{124}Te	1.00, 1.00	
^{124}Te	−0.68			^{85}Kr(n, γ)^{86}Kr			1.00, 1.00	
	−0.45	−0.69			^{124}Te(n, γ)^{125}Te		1.00, 1.00	
	0.17	0.22	0.81			^{86}Kr(n, γ)^{87}Kr	1.00, 1.00	
^{126}Te	−0.60	−0.80			^{126}Te(n, γ)^{127}Te		1.00, 1.00	
	0.14	0.17	0.83			^{86}Kr(n, γ)^{87}Kr	1.00, 1.00	
^{127}I	−0.87			^{127}I(n, γ)^{128}I			1.00, 0.99	
	0.09	0.28	0.83			^{86}Kr(n, γ)^{87}Kr	1.00, 1.00	
^{128}Xe	0.57	0.72			^{128}I(β^-)^{128}Xe			1.64, 5.42
	−0.22	−0.27	−0.69			^{128}I(β^+)^{128}Te		
^{130}Xe	−0.67			^{85}Kr(n, γ)^{86}Kr			1.00, 1.00	
	−0.44	−0.67			^{130}Xe(n, γ)^{131}Xe		1.00, 1.00	
	0.16	0.19	0.86			^{86}Kr(n, γ)^{87}Kr	1.00, 1.00	
^{132}Xe	−0.94			^{132}Xe(n, γ)^{133}Xe			1.00, 1.00	
	0.05	0.23	0.87			^{86}Kr(n, γ)^{87}Kr	1.00, 1.00	
^{133}Cs	−0.80			^{133}Cs(n, γ)^{134}Cs			1.00, 1.00	
	0.12	0.23	0.87			^{86}Kr(n, γ)^{87}Kr	1.00, 1.00	
^{134}Ba	−0.75			^{134}Ba(n, γ)^{135}Ba			1.00, 1.00	
	0.10	0.22	0.73			^{86}Kr(n, γ)^{87}Kr	1.00, 1.00	
^{136}Ba	−0.78			^{136}Ba(n, γ)^{137}Ba			1.00, 1.00	
	0.10	0.20	0.87			^{86}Kr(n, γ)^{87}Kr	1.00, 1.00	
^{137}Ba	−0.72			^{137}Ba(n, γ)^{138}Ba			1.00, 1.00	
	0.12	0.19	0.87			^{86}Kr(n, γ)^{87}Kr	1.00, 1.00	
^{138}Ba	−0.87			^{138}Ba(n, γ)^{139}Ba			1.00, 1.00	
	0.23	0.65			^{64}Ni(n, γ)^{65}Ni		1.00, 1.00	
^{139}La	−0.96			^{139}La(n, γ)^{140}La			1.00, 1.00	
	0.11	0.65			^{64}Ni(n, γ)^{65}Ni		1.00, 1.00	
^{140}Ce	−0.84			^{140}Ce(n, γ)^{141}Ce			1.00, 1.00	

Table A3 *– continued*

Nuclide	$r_{cor,0}$	$r_{cor,1}$	$r_{cor,2}$	Key rate Level 1	Key rate Level 2	Key rate Level 3	X_0 (8, 30 keV)	β-decay
^{142}Nd	−0.73			^{142}Nd(n, γ)^{143}Nd			1.00, 1.00	
^{144}Nd	−0.66			^{144}Nd(n, γ)^{145}Nd			1.00, 1.00	
^{146}Nd	−0.26	−0.42	−0.69			^{146}Nd(n, γ)^{147}Nd	1.00, 1.00	
^{147}Sm	−0.31	−0.50	−0.76			^{147}Sm(n, γ)^{148}Sm	1.00, 1.00	
^{148}Sm	−0.29	−0.48	−0.73			^{148}Sm(n, γ)^{149}Sm	1.00, 1.00	
^{150}Sm	0.66			^{138}Ba(n, γ)^{139}Ba			1.00, 1.00	
^{151}Eu	−0.93			^{151}Eu(n, γ)^{152}Eu			0.89, 0.79	
^{153}Eu	−0.32	−0.57	−0.80			^{153}Eu(n, γ)^{154}Eu	1.00, 1.00	
^{152}Gd	0.80			^{151}Sm(β^-)^{151}Eu				3.60, 5.42
	−0.16	−0.74			^{151}Sm(n, γ)^{152}Sm		0.80, 0.76	
^{156}Gd	−0.51	−0.73			^{156}Gd(n, γ)^{157}Gd		1.00, 0.99	
^{158}Gd	−0.65			^{158}Gd(n, γ)^{159}Gd			1.00, 0.98	
^{159}Tb	−0.97			^{159}Tb(n, γ)^{160}Tb			1.00, 0.98	
^{160}Dy	−0.65			^{160}Dy(n, γ)^{161}Dy			1.00, 0.99	
^{162}Dy	−0.69			^{162}Dy(n, γ)^{163}Dy			1.00, 0.98	
^{164}Dy	−0.80			^{164}Dy(n, γ)^{165}Dy			1.00, 0.97	
^{165}Ho	−0.95			^{165}Ho(n, γ)^{166}Ho			1.00, 1.00	
^{166}Er	−0.97			^{166}Er(n, γ)^{167}Er			1.00, 0.98	
^{167}Er	−0.97			^{167}Er(n, γ)^{168}Er			1.00, 1.00	
^{168}Er	−0.98			^{168}Er(n, γ)^{169}Er			1.00, 0.98	
^{169}Tm	−0.97			^{169}Tm(n, γ)^{170}Tm			0.51, 0.42	
^{170}Yb	−0.64	−0.84			^{170}Yb(n, γ)^{171}Yb		1.00, 0.99	
^{172}Yb	−0.71			^{172}Yb(n, γ)^{173}Yb			1.00, 0.98	
^{174}Yb	−0.72			^{174}Yb(n, γ)^{175}Yb			1.00, 0.98	
^{175}Lu	0.70			^{138}Ba(n, γ)^{139}Ba			1.00, 1.00	
^{176}Lu	0.66			^{138}Ba(n, γ)^{139}Ba			1.00, 1.00	
^{176}Hf	0.90			^{176}Lu(β^-)^{176}Hf				1.30, 1.33
	−0.11	−0.48	−0.69			^{176}Hf(n, γ)^{177}Hf	1.00, 0.99	
^{178}Hf	−0.48	−0.72			^{178}Hf(n, γ)^{179}Hf		1.00, 0.99	
^{180}Hf	−0.53	−0.78			^{180}Hf(n, γ)^{181}Hf		1.00, 0.99	
^{181}Ta	−0.98			^{181}Ta(n, γ)^{182}Ta			0.61, 0.55	
^{182}W	−0.77			^{182}W(n, γ)^{183}W			1.00, 1.00	
^{183}W	−0.91			^{183}W(n, γ)^{184}W			0.99, 0.93	
^{184}W	−0.58	−0.83			^{184}W(n, γ)^{185}W		1.00, 1.00	
^{185}Re	−0.80			^{185}Re(n, γ)^{186}Re			1.00, 1.00	
^{186}Os	−0.74			^{186}Os(n, γ)^{187}Os			1.00, 1.00	
	0.34	0.68			^{186}Re(β^-)^{186}Os			1.30, 3.59
	−0.21	−0.43	−0.77			^{186}Re(β^+)^{186}W		
^{187}Os	−0.97			^{187}Os(n, γ)^{188}Os			0.57, 0.46	
	0.07	0.67			^{186}Re(β^-)^{186}Os			1.30, 3.59
	−0.05	−0.43	−0.76			^{186}Re(β^+)^{186}W		
^{188}Os	−0.84			^{188}Os(n, γ)^{189}Os			1.00, 1.00	
^{190}Os	−0.78			^{190}Os(n, γ)^{191}Os			1.00, 1.00	
^{191}Ir	−0.62	−0.86			^{191}Ir(n, γ)^{192}Ir		1.00, 1.00	
^{193}Ir	−0.90			^{193}Ir(n, γ)^{194}Ir			1.00, 0.99	
	−0.31	−0.91			^{193}Pt(n, γ)^{194}Pt		0.25, 0.21	
^{192}Pt	−0.96			^{192}Pt(n, γ)^{193}Pt			1.00, 1.00	
	0.04	0.74			^{192}Ir(β^-)^{192}Pt			1.31, 6.36
^{194}Pt	−0.94			^{194}Pt(n, γ)^{195}Pt			1.00, 1.00	
	−0.04	−0.73			^{193}Pt(n, γ)^{194}Pt		0.25, 0.21	
^{196}Pt	−0.96			^{196}Pt(n, γ)^{197}Pt			1.00, 1.00	
^{197}Au	0.73			^{138}Ba(n, γ)^{139}Ba			1.00, 1.00	
^{198}Hg	−0.96			^{198}Hg(n, γ)^{199}Hg			1.00, 1.00	
^{200}Hg	−0.97			^{200}Hg(n, γ)^{201}Hg			1.00, 1.00	
^{202}Hg	−0.77			^{202}Hg(n, γ)^{203}Hg			1.00, 1.00	
^{203}Tl	−0.94			^{203}Tl(n, γ)^{204}Tl			1.00, 1.00	
^{205}Tl	−0.94			^{205}Pb(n, γ)^{206}Pb			0.83, 0.82	
^{204}Pb	−0.84			^{204}Pb(n, γ)^{205}Pb			1.00, 1.00	
^{206}Pb	−0.59	−0.88			^{206}Pb(n, γ)^{207}Pb		1.00, 1.00	
^{207}Pb	−0.64	−0.81			^{207}Pb(n, γ)^{208}Pb		1.00, 1.00	
^{209}Bi	0.68			^{208}Pb(n, γ)^{209}Pb			1.00, 1.00	
	−0.36	−0.57	−0.95			^{209}Bi(n, γ)^{210}Bi	1.00, 1.00	

Table A4. The key reaction rates for the TP model. Key rates in levels 1−3 are shown, along with their correlation factors r_{cor0}, r_{cor1}, and r_{cor2}, respectively. Not all s-process nuclides analysed are listed but only those for which key rates were found. Also shown for each rate are the ground state contributions X_0 to the stellar rate of the (n,γ) reaction and uncertainty factors of the β-decay rate at two plasma temperatures, respectively.

Nuclide	$r_{cor,0}$	$r_{cor,1}$	$r_{cor,2}$	Key rate Level 1	Key rate Level 2	Key rate Level 3	X_0 (8, 30 keV)	β-decay
^{70}Ge	−0.83			^{70}Ge(n, γ)^{71}Ge			1.00, 1.00	
	0.41	0.73			^{68}Zn(n, γ)^{69}Zn		1.00, 1.00	
	0.36	0.67			^{69}Ga(n, γ)^{70}Ga		1.00, 1.00	
	−0.04	−0.11	−0.94			^{70}Ga(n, γ)^{71}Ga	1.00, 1.00	
^{76}Se	0.76			^{74}Ge(n, γ)^{75}Ge			1.00, 1.00	
	−0.59	−0.90			^{76}Se(n, γ)^{77}Se		1.00, 1.00	
	0.27	0.37	0.84			^{75}As(n, γ)^{76}As	1.00, 1.00	
^{82}Se	0.88			^{81}Se(n, γ)^{82}Se			1.00, 1.00	
	−0.30	−0.83			^{82}Se(n, γ)^{83}Se		1.00, 1.00	
	−0.27	−0.46	−0.85			^{81}Se(β^-)^{81}Br		1.30, 2.17
^{80}Kr	0.66			^{80}Br(β^-)^{80}Kr				1.31, 4.70
	−0.47	−0.66			^{80}Kr(n, γ)^{81}Kr		1.00, 1.00	
^{86}Sr	−0.92			^{86}Sr(n, γ)^{87}Sr			1.00, 1.00	
	−0.27	−0.71			^{86}Rb(n, γ)^{87}Rb		1.00, 1.00	
	0.15	0.39	0.89			^{85}Rb(n, γ)^{86}Rb	1.00, 1.00	
^{87}Sr	0.65			^{86}Sr(n, γ)^{87}Sr			1.00, 1.00	
	−0.75			^{87}Sr(n, γ)^{88}Sr			1.00, 1.00	
	0.04	0.44	0.76			^{85}Rb(n, γ)^{86}Rb	1.00, 1.00	
^{96}Zr	−0.74			^{95}Zr(β^-)^{95}Nb				
	0.46	0.98			^{95}Zr(n, γ)^{96}Zr		1.00, 1.00	
	0.06	0.13	0.95			^{94}Zr(n, γ)^{95}Zr	1.00, 1.00	
^{94}Mo	−0.80			^{94}Mo(n, γ)^{95}Mo			1.00, 1.00	
	−0.43	−0.71			^{94}Nb(n, γ)^{95}Nb		0.99, 0.97	
	0.33	0.56	0.81			^{94}Nb(β^-)^{94}Mo		1.35, 3.22
^{96}Mo	−0.66			^{96}Mo(n, γ)^{97}Mo			1.00, 1.00	
^{100}Mo	0.85			^{99}Mo(n, γ)^{100}Mo			1.00, 1.00	
	−0.42	−0.82			^{99}Mo(β^-)^{99}Tc			1.30, 2.13
	−0.14	−0.32	−1.00			^{100}Mo(n, γ)^{101}Mo	1.00, 1.00	
^{100}Ru	−0.79			^{100}Ru(n, γ)^{101}Ru			1.00, 1.00	
	0.57	0.95			^{98}Mo(n, γ)^{99}Mo		1.00, 1.00	
	0.18	0.29	0.91			^{99}Tc(n, γ)^{100}Tc	1.00, 1.00	
^{104}Ru	0.65			^{103}Ru(n, γ)^{104}Ru			0.45, 0.41	
	−0.49	−0.67			^{103}Ru(β^-)^{103}Rh			5.76, 6.34
	−0.06	−0.06	−0.98			^{104}Ru(n, γ)^{105}Ru	1.00, 1.00	
^{104}Pd	−0.95			^{104}Pd(n, γ)^{105}Pd			1.00, 1.00	
	0.20	0.69			^{102}Ru(n, γ)^{103}Ru		1.00, 1.00	
	0.20	0.66			^{103}Rh(n, γ)^{104}Rh		0.95, 0.80	
^{110}Pd	0.86			^{109}Pd(n, γ)^{110}Pd			1.00, 1.00	
^{110}Cd	0.87			^{108}Pd(n, γ)^{109}Pd			1.00, 1.00	
	0.31	0.75			^{106}Pd(n, γ)^{107}Pd		1.00, 1.00	
	0.20	0.47	0.72			^{109}Ag(n, γ)^{110}Ag	1.00, 1.00	
^{116}Cd	0.96			^{115}Cd(n, γ)^{116}Cd			1.00, 1.00	
	−0.26	−0.96			^{115}Cd(β^-)^{115}In			1.30, 1.44
^{114}Sn	0.66			^{113}Sn(n, γ)^{114}Sn			1.00, 0.99	
	0.55	0.77			^{112}Sn(n, γ)^{113}Sn		1.00, 1.00	
^{115}Sn	0.67			^{113}Sn(n, γ)^{114}Sn			1.00, 0.99	
	−0.45	−0.59	−0.66			^{115}Sn(n, γ)^{116}Sn	1.00, 1.00	
^{116}Sn	0.81			^{115}In(n, γ)^{116}In			1.00, 1.00	
	−0.27	−0.82			^{116}Sn(n, γ)^{117}Sn		1.00, 1.00	
	−0.15	−0.42	−0.89			^{116}In(n, γ)^{117}In	1.00, 1.00	
^{124}Sn	0.96			^{123}Sn(n, γ)^{124}Sn			0.98, 0.96	
^{122}Te	0.74			^{121}Sb(n, γ)^{122}Sb			0.98, 0.93	
^{123}Te	−0.60	−0.78			^{123}Te(n, γ)^{124}Te		1.00, 1.00	
^{124}Te	0.87			^{121}Sb(n, γ)^{122}Sb			0.98, 0.93	
	−0.37	−0.71			^{124}Te(n, γ)^{125}Te		1.00, 1.00	
^{130}Te	−0.78			^{130}I(β^-)^{130}Xe				1.31, 4.97
^{128}Xe	0.75			^{128}I(β^-)^{128}Xe				1.64, 5.42
	0.31	0.66			^{127}I(n, γ)^{128}I		1.00, 0.99	
^{130}Xe	0.83			^{129}Xe(n, γ)^{130}Xe			0.98, 0.90	
	0.32	0.67			^{127}I(n, γ)^{128}I		1.00, 0.99	
	−0.25	−0.58	−0.79			^{130}Xe(n, γ)^{131}Xe	1.00, 1.00	

Table A4 – *continued*

Nuclide	$r_{cor,0}$	$r_{cor,1}$	$r_{cor,2}$	Key rate Level 1	Key rate Level 2	Key rate Level 3	X_0 (8, 30 keV)	β-decay
^{134}Xe	−0.68			^{134}Cs(β^-)^{134}Ba				3.24, 5.52
	0.39	0.83			^{133}Xe(n, γ)^{134}Xe		1.00, 1.00	
	−0.10	−0.20	−0.70			^{133}Xe(β^-)^{133}Cs		1.30, 1.30
	0.08	0.15	0.66			^{131}Xe(n, γ)^{132}Xe	1.00, 1.00	
^{136}Xe	−0.66			^{134}Cs(β^-)^{134}Ba				3.24, 5.52
	0.39	0.86			^{134}Cs(n, γ)^{135}Cs		0.78, 0.68	
	−0.19	−0.40	−0.90			^{136}Cs(β^-)^{136}Ba		
^{134}Ba	0.64	0.72			^{132}Xe(n, γ)^{133}Xe		1.00, 1.00	
	−0.38	−0.40	−0.77			^{134}Ba(n, γ)^{135}Ba	1.00, 1.00	
^{136}Ba	−0.82			^{136}Ba(n, γ)^{137}Ba			1.00, 1.00	
	0.37	0.64	0.71			^{134}Ba(n, γ)^{135}Ba	1.00, 1.00	
^{138}La	−0.94			^{138}La(n, γ)^{139}La			1.00, 1.00	
	0.14	0.66			^{137}La(n, γ)^{138}La		0.87, 0.80	
	0.07	0.32	0.82			^{136}Ce(n, γ)^{137}Ce	1.00, 1.00	
^{142}Ce	−0.69			^{141}Ce(β^-)^{141}Pr				
	0.40	0.93			^{141}Ce(n, γ)^{142}Ce		1.00, 1.00	
^{148}Nd	−0.68			^{147}Nd(β^-)^{147}Pm				1.30, 3.03
	0.65			^{147}Nd(n, γ)^{148}Nd			1.00, 0.98	
	−0.05	−0.66			^{56}Fe(n, γ)^{57}Fe		1.00, 1.00	
	−0.02	−0.67			^{57}Fe(n, γ)^{58}Fe		0.73, 0.59	
^{148}Sm	0.48	0.65			^{148}Pm(β^-)^{148}Sm			1.30, 2.77
	0.35	0.70			^{147}Pm(n, γ)^{148}Pm		1.00, 1.00	
^{150}Sm	0.66			^{148}Pm(n, γ)^{149}Pm			1.00, 1.00	
	0.47	0.73			^{147}Pm(n, γ)^{148}Pm		1.00, 1.00	
	0.07	0.13	0.91			^{149}Sm(n, γ)^{150}Sm	0.97, 0.93	
^{152}Sm	−0.76			^{152}Sm(n, γ)^{153}Sm			1.00, 1.00	
	0.13	0.31	0.95			^{149}Sm(n, γ)^{150}Sm	0.97, 0.93	
^{152}Gd	0.93			^{151}Sm(β^-)^{151}Eu				3.60, 5.42
	−0.31	−0.89			^{151}Sm(n, γ)^{152}Sm		0.80, 0.76	
^{154}Gd	−0.75			^{154}Gd(n, γ)^{155}Gd			1.00, 1.00	
^{160}Gd	0.81			^{159}Gd(n, γ)^{160}Gd			1.00, 0.97	
^{160}Dy	−0.85			^{160}Dy(n, γ)^{161}Dy			1.00, 0.99	
^{170}Er	−0.66			^{169}Er(β^-)^{169}Tm				1.30, 4.46
	0.55	0.90			^{169}Er(n, γ)^{170}Er		1.00, 0.98	
	0.21	0.34	0.80			^{168}Er(n, γ)^{169}Er	1.00, 0.98	
^{170}Yb	−0.85			^{170}Tm(n, γ)^{171}Tm			0.98, 0.91	
^{176}Yb	0.90			^{175}Yb(n, γ)^{176}Yb			1.00, 1.00	
	−0.26	−0.84			^{175}Yb(β^-)^{175}Lu			1.30, 1.58
	−0.15	−0.48	−0.98			^{176}Yb(n, γ)^{177}Yb	1.00, 0.98	
^{176}Lu	0.85			^{174}Yb(n, γ)^{175}Yb			1.00, 0.98	
	−0.37	−0.72			^{176}Lu(β^-)^{176}Hf			1.30, 1.33
	0.30	0.55	0.83			^{172}Yb(n, γ)^{173}Yb	1.00, 0.98	
^{186}W	−0.83			^{185}W(β^-)^{185}Re				1.44, 3.87
	0.31	0.71			^{185}W(n, γ)^{186}W		0.98, 0.95	
^{187}Re	−0.54	−0.62	−0.68			^{186}Re(β^-)^{186}Os		1.30, 3.59
^{186}Os	0.72			^{185}W(β^-)^{185}Re				1.44, 3.87
	−0.43	−0.67			^{186}Os(n, γ)^{187}Os		1.00, 1.00	
^{187}Os	−0.88			^{187}Os(n, γ)^{188}Os			0.57, 0.46	
	0.14	0.58	0.67			^{186}Re(β^-)^{186}Os		1.30, 3.59
^{192}Os	0.85			^{191}Os(n, γ)^{192}Os			1.00, 1.00	
	−0.44	−0.82			^{191}Os(β^-)^{191}Ir			1.30, 1.76
	−0.17	−0.35	−0.71			^{192}Os(n, γ)^{193}Os	1.00, 1.00	
^{192}Pt	−0.69			^{192}Pt(n, γ)^{193}Pt			1.00, 1.00	
	−0.56	−0.81			^{192}Ir(n, γ)^{193}Ir		0.64, 0.51	
	0.33	0.50	0.90			^{192}Ir(β^-)^{192}Pt		1.31, 6.36
^{195}Pt	−0.91			^{195}Pt(n, γ)^{196}Pt			1.00, 1.00	
	0.22	0.88			^{194}Pt(n, γ)^{195}Pt		1.00, 1.00	
^{198}Pt	0.91			^{197}Pt(n, γ)^{198}Pt			0.99, 0.94	
	−0.27	−0.71			^{197}Pt(β^-)^{197}Au			1.31, 4.90
	−0.06	−0.20	−1.00			^{198}Pt(n, γ)^{199}Pt	1.00, 1.00	
^{198}Hg	−0.70			^{198}Hg(n, γ)^{199}Hg			1.00, 1.00	
	0.49	0.78			^{196}Pt(n, γ)^{197}Pt		1.00, 1.00	
	−0.11	−0.17	−0.76			^{198}Au(n, γ)^{199}Au	1.00, 1.00	

Table A4 – *continued*

Nuclide	$r_{cor,0}$	$r_{cor,1}$	$r_{cor,2}$	Key rate Level 1	Key rate Level 2	Key rate Level 3	X_0 (8, 30 keV)	β-decay
^{204}Pb	0.76			^{203}Tl(n, γ)^{204}Tl			1.00, 1.00	
	−0.47	−0.74			^{204}Tl(n, γ)^{205}Tl		1.00, 1.00	
	−0.38	−0.59	−0.89			^{204}Pb(n, γ)^{205}Pb	1.00, 1.00	
^{209}Bi	0.94			^{208}Pb(n, γ)^{209}Pb			1.00, 1.00	
	−0.32	−0.91			^{209}Bi(n, γ)^{210}Bi		1.00, 1.00	

This paper has been typeset from a TEX/LATEX file prepared by the author.